Changes in the Length of the Season with Favorable Environmental Conditions for Tropical Cyclones in the North Atlantic Basin during the Last 40 Years

Yanjie $Wu^{a,b}$ and Robert L. Korty b

^a Ocean University of China, Qingdao, Shandong, China ^b Texas A&M University, College Station, Texas

(Manuscript received 29 September 2021, in final form 10 March 2022)

ABSTRACT: Analyses of two high-resolution reanalysis products show that high values of hurricane potential intensity (PI) are becoming more frequent and covering a larger area of the Atlantic, which is consistent with the lengthening of the tropical cyclone season previously reported. These changes are especially pronounced during the early months of the storm season (May–July) in subtropical latitudes. The western subtropical Atlantic features increases in mean PI as well as the areal coverage and frequency of high PI throughout the storm season; the length of the season with high PI has grown since 1980. The number of days with low vertical wind shear increases in the tropical North Atlantic during the early and middle months of the storm season, but trends are mixed and generally insignificant elsewhere. A thermodynamic parameter measuring the ratio of midlevel entropy deficits to the strength of surface fluxes that work to eliminate them is sensitive to the choice of the pressure level(s) used to calculate its value in the boundary layer, as well as to subtle differences in temperature and humidity values near the surface in different reanalysis datasets, leading to divergent results in metrics like the ventilation index that depend on its value. Projections from a high-resolution simulation of the remainder of the twenty-first century show that the number of days with high PI is likely to continue increasing in the North Atlantic basin, with trends especially strong in the western subtropical Atlantic during the early and late months of the season.

KEYWORDS: Tropical cyclones; North Atlantic Ocean; Hurricanes/typhoons

1. Introduction

Assessing whether, how, and why aspects of the observed record of tropical cyclones change can be a deceptively difficult problem. Historical records of tropical cyclones have been constructed from disparate observational methodologies that have varied with changing technology over time, and they often required subjective judgements made by different forecasters across the world (e.g., Landsea et al. 2006; Vecchi et al. 2021). If limited to the past four decades, some of these concerns can be diminished by using a globally homogeneous satellite record spanning the 40 years of global coverage (Kossin et al. 2013, 2014), making this period the most thoroughly documented and observed. Kossin (2008) reported that during this period the length of the tropical cyclone storm season (as measured by the first and last dates of named storm activity) underwent a statistically significant increase of about 1 day yr⁻¹ in the North Atlantic basin. This particular finding, however, appears sensitive to the period and geographic area included in the analysis, as Karloski and Evans (2016) reported when they revisited these results through the 2014 season: they found no statistically significant change when the analysis extended to the full basin [a wider geographic area than Kossin (2008) used]. Dwyer et al. (2015) found mixed trends in simulations of future climate change, but they argued that increases

© Supplemental information related to this paper is available at the Journals Online website: https://doi.org/10.1175/JCLI-D-21-0767.s1.

Corresponding author: Yanjie Wu, wuyanjie@stu.ouc.edu.cn

in storm counts in a given year tended to drive an increase in the length of the season from start to finish. Dwyer et al. (2012, 2014) also reported that annual cycles of tropical sea surface temperatures (SSTs) and precipitation increase in amplitude and peaks shift later in the season in climate model projections forced with rising greenhouse gases. However, tropical cyclones do not respond directly to absolute SST changes, but rather to potential intensity, which depends on the relationship between SST and the atmospheric thermal profile in the column above it (e.g., Emanuel 1987; Royer et al. 1998; Emanuel and Sobel 2013).

In a series of pioneering papers, Gray (1968, 1975, 1979) showed that there are particular large-scale properties common to the genesis regions of tropical cyclones globally. Among these are warm SST, atmospheric thermal profiles supporting deep convection, low deep-layer vertical wind shear, high relative humidity, and elevated low-level absolute vorticity. These environmental factors are generally regarded as necessary conditions for tropical cyclone (TC) formation, although later work has refined our understanding of how they permit or limit development and intensification. An important example is that although TCs in the modern climate are rarely observed to form over water colder than 26°C (Palmén 1948; Gray 1968), there is no threshold SST required to create a TC; rather, high potential intensity (Emanuel 1986; Bister and Emanuel 2002) is required (Emanuel 1987; Royer et al. 1998; Korty et al. 2017). Similarly, while elevated low-level vorticity is likely important for the formation of individual TCs, Tippett et al. (2011) showed that vorticity is not generally a rate-limiting factor outside of very low latitudes.

Genesis indices constructed from an updated set of parameters like these (see section 2 for additional details) have proven remarkably useful in studies of TCs and climate (e.g., Emanuel 2010;

DOI: 10.1175/JCLI-D-21-0767.1

Tippett et al. 2011; McGauley and Nolan 2011; Menkes et al. 2012; Tang and Emanuel 2012). These indices are constructed empirically by maximizing the statistical relationship between observed TCs and values of environmental conditions, and they have also proven useful in studies of model projected climate changes and TC activity. For TCs statistically downscaled from the large-scale properties of climate models (Emanuel et al. 2008), these environmental parameters control the response across a wide range of climate states (e.g., Emanuel 2010, 2013, 2021; Korty et al. 2017; Lawton et al. 2021), but the relationship between TCs generated by a climate model and these environmental parameters is more complex. Camargo et al. (2020) undertook a comprehensive examination of the TC-like vortices generated in 30 climate models with varying horizontal resolution. They found that there was no universal relationship between a model's number of modelgenerated storms and the model's representation of environmental conditions. (For example, if a particular model has a mean state with potential intensity values above what occurs in other models, it does not necessarily generate more storms than those other models.) The Camargo et al. (2020) results do not imply there are no relationships 1) between TC activity in a particular model and interannual variability in that model's simulated environmental conditions or 2) between TC activity and changes in a model's environmental conditions due to climate change. Their analysis showed that there is no universal threshold to these parameter values common from one model to another and that there may be especially weak relationships between environmental conditions and model-generated storms in coarse resolution models. In higher-resolution models (with horizontal resolution from 0.25° to 1.25°), Camargo et al. (2020) found that there is a significant relationship between the magnitude of vertical wind shear and storm development.

In this paper, we are motivated by the increase since the 1980s of storm activity during the early and late parts of the season, as shown in Fig. 1. The genesis date of the first named TC from the best track data (see section 2 and Fig. 1) has moved earlier by about 2 weeks decade⁻¹, consistent with results first reported by Kossin (2008). (Here we choose to mark the start of each year on 1 March, so that the rare January event is defined to be a part of the prior calendar year's season; no storms have formed during February or March, making this a sensible breakpoint roughly 6 months from the Atlantic season's peak.) This shift to earlier formation is also seen in a broader metric, the 10th percentile of storm days, whose time series is constructed by adding one to each date if any storm existed in the basin. There is a smaller shift in the date of last storm to form and in the 90th percentile of storm days (Fig. 1b), but the linear trend from 1980 to 2019 is not statistically significant. The shift to longer seasons between 1980 and 2019 (16.47 days decade⁻¹ with p = 0.01) has occurred in conjunction with an increase in total storms, consistent with the arguments of Dwyer et al. (2015). Figures 1c and 1d show the annual time series of the data extended to 1950, which reveals that the changes since 1980 are perhaps better viewed as a recovery from a drought of activity during the 1970s and 1980s and are concurrent with a warmer state of Atlantic multidecadal variability. Our goal in this paper is to investigate whether the changes in early and late season

activity that have occurred since then are accompanied by related changes in the spatial coverage and temporal frequency of favorable environmental conditions during early, middle, and late months of the season. We constrain our primary analysis to the period between 1980 and 2019, which overlaps with the global satellite coverage and allows a comparison of some reanalysis products that span only this interval; this period spans the recovery of TC activity from its basinwide drought.

2. Data and background

a. Reanalysis data

To construct the time series of historical data shown in Fig. 1, we used the best track hurricane dataset (HURDAT2) from the National Hurricane Center. Cyclones are included only for the portion of their lifetime that their maximum wind speed exceeds 17 m s⁻¹ (tropical storm intensity and stronger). As mentioned in section 1, we choose to define the start of each "year" on 1 March, which makes the occasional January storm a part of the prior calendar year's season. We favor this definition because 1) the annual transition occurs during the middle of the winter-spring cyclone drought (no storms form during February or March), 2) it is roughly 6 months from the peak of activity in the Atlantic, and 3) several years with January activity follow active seasons, suggesting that activity in that month might often be thought of as an extension of the prior year's season extending across 1 January into a new calendar year.

We construct environmental factors from daily-averaged temperature, humidity, and horizontal wind component data from two high-resolution reanalysis datasets. The fifth generation of the European Centre for Medium-Range Weather Forecasts (ECMWF) atmospheric reanalysis (ERA5) offers high spatial resolution and the data used here are from a 0.25° longitude \times 0.25° latitude grid. The National Aeronautics and Space Administration (NASA) Modern-Era Retrospective Analysis for Research and Applications, version 2 (MERRA-2) was generated using the NASA Goddard Earth Observing System (GEOS) data assimilation system, and provides data beginning in 1980 (Gelaro et al. 2017). The horizontal resolution of the MERRA-2 data is 0.625° longitude \times 0.5° latitude. These (and several other) reanalysis products provide fields on regular spatial grids and at regular temporal intervals, have a wide selection of variables calculated using internally consistent methods, and assimilate a large range of measurements, both in situ and remotely sensed. These features have rendered them very useful and attractive datasets, although comparisons with direct measurements are necessary to reveal their strengths and weaknesses; prior studies have compared these datasets (and their predecessors, MERRA and ERA-Interim) with field campaigns over the tropical North Atlantic (e.g., Vergados et al. 2014; Robertson et al. 2016; Guan et al. 2018; Luo et al. 2020). Both MERRA-2 and ERA-5 include daily SST as an input variable to their reanalyses, and Luo et al. (2020) recently compared their boundary layer temperature and humidity profiles to data collected in the tropical North Atlantic during a series of research cruises (Morris et al. 2006; Nalli et al. 2011). We choose

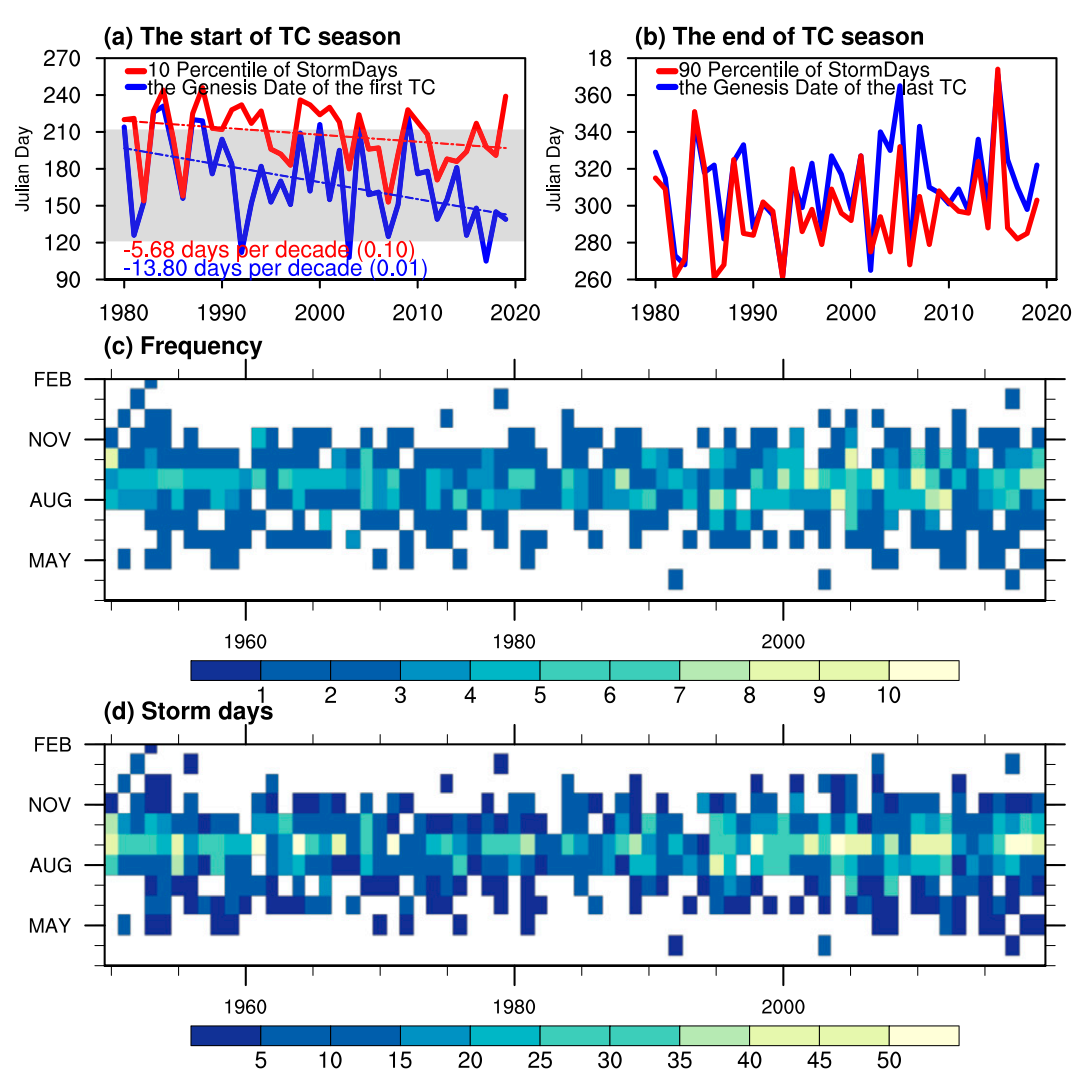


FIG. 1. (a) The Julian day of the first day of genesis (blue) and the 10th percentile of storm days (red) of tropical cyclone (TC) activity in the North Atlantic (NA) from 1980 to 2019 using the best track data from the National Hurricane Center. (b) The Julian day of the last date of genesis (blue) and the 90th percentile of storm days (red) of TC activity in the NA. (c) Frequency of storm genesis in each month of the year. (d) Number of storm days in each month of the year. Statistically significant trend lines for the data in (a) are shown with p value in parentheses, and the gray shading high-lights the period from 1 May to 31 Jul, which we define as the early (and preseason) months in the paper.

these two datasets for our analysis to capitalize on the prior work done with them and to show some of the sensitivity in calculations of tropical cyclone environmental factors that can arise from seemingly small differences in the values of boundary layer fields.

b. Climate model data

We also analyze how environmental variables change during early and preseason months (May–July), peak months of the Atlantic season (August–October), and in late and postseason months (November and December) in high-resolution simulations of the second half of the twentieth century and in projections of the remainder of the twenty-first century, which follow protocols of the Coupled Model Intercomparison Project

phase 6 CMIP6 (Eyring et al. 2016) and data output requirements of the HighResMIP CMIP6 (Haarsma et al. 2016). Knutson et al. (2010) among many others have shown that external forces can have profound effects on TC activity, and we use a coupled high-resolution (25 km) simulation of CESM from 1950 to 2100 to assess how the annual cycle of favorable environmental conditions evolves under the projections of further anthropogenic change. The simulation is forced using historical emissions for the period from 1950 to 2014 and by projections using the representative concentration pathway 8.5 (RCP8.5) from 2015 to 2100; note that the years that overlap with those of the reanalysis data are a mixture of forcing by historical emissions (until 2014) and RCP8.5 projections (2015 forward). Li et al. (2020) showed that the improved boundary layer

physics and representations of air–sea and air–land interactions offered by high-resolution simulations leads to improved predictability of TC genesis.

c. Environmental factors

Tropical cyclones require conditions in the large-scale environments to be conducive for development (e.g., Gray 1975) and intensification. Several decades of work have gone into identifying the measures of environmental properties and combinations of them that best relate to tropical cyclone climatology, but generally these environmental factors and the indices derived from them include both kinematic and thermodynamic measures of the large-scale flow. Below we briefly review and justify the parameters used in this paper, although more comprehensive discussions have been taken up by Tippett et al. (2011), McGauley and Nolan (2011), Nolan (2011), Bruyère et al. (2012), and Korty et al. (2012a,b), among others.

1) INDIVIDUAL FACTORS

Deep-layer vertical wind shear (VWS) is defined here as the magnitude of the vector difference between the 250- and 850-hPa horizontal wind vectors. [Many studies define VWS as the difference in winds between 200 and 850 hPa (e.g., Wong and Chan 2004; Kim et al. 2009; Zheng et al. 2020), but other papers define the upper level using 250 hPa (e.g., Korty et al. 2017; Li et al. 2020) or 300 hPa (e.g., Gualdi et al. 2008) instead. The qualitative conclusions of our analysis are insensitive to the choice of upper-tropospheric pressure level, and we choose 250 hPa to be able in future work to compare with statistically downscaled results (e.g., Emanuel et al. 2008; Korty et al. 2017; Lawton et al. 2021) that use this level.] Strong VWS hinders the genesis and development of TCs not only by disrupting the vertical alignment of a developing circulation, but also thermodynamically via ventilation of ambient dry air into the developing convective core (Tang and Neelin 2004; Tang and Emanuel 2012).

Potential intensity (PI; Emanuel 1986; Bister and Emanuel 1998) defines a thermodynamic limit on TC intensity based on a steady-state balance between a cyclone's acquisition of energy from ocean surface fluxes and the dissipation of a cyclone's wind field against dissipative sinks. It is a fundamental property of TC environments, because while warm sea surface temperatures (SSTs) are found where TCs form (Palmén 1948; Gray 1968), there is no common threshold SST for TC formation across climates (Emanuel 1987; Royer et al. 1998; Korty et al. 2017; Lawton et al. 2021). Rather, the common element in TC formation is high PI (Korty et al. 2012b): PI can only be large if the atmosphere supports deep convection of surface parcels heated by surface enthalpy fluxes. If the thermodynamic sounding does not (e.g., by low- or midtropospheric temperature inversion in the column) support it, PI is low and TCs cannot be maintained [see section 3 of Korty et al. (2012b) for further discussion]. We calculate PI using an algorithm first devised by Bister and Emanuel (2002):

$$PI = \left[\frac{C_K}{C_D} \frac{SST}{T_o} (CAPE^* - CAPE^b)\right]^{1/2}.$$
 (1)

Here CAPE^{*} is the convective available potential energy (CAPE) of an air parcel lifted from saturation at the sea level pressure in reference to the local environmental sounding, CAPE^b is the CAPE of an ambient boundary layer parcel, SST is the sea surface temperature (in kelvins), T_o is the temperature at the level of convective outflow (found iteratively using the algorithm), and C_K and C_D are exchange coefficients for enthalpy and drag, respectively (their ratio is set to 0.9 here).

Gray (1975) understood that midtropospheric levels of humidity were important to TC development. Higher midlevel humidity reduces the amount of water required to bring a column to saturation, and higher ambient humidity levels also reduce the dryness of air brought down to the surface by convective downdrafts during the genesis process (Nolan 2011). The nondimensional ratio of the strength of the convective entropy flux to that of the surface entropy flux proved important in axisymmetric hurricane models (Emanuel 1989, 1995), and this parameter is defined as

$$\chi = \frac{s_b - s_m}{s_c^* - s_b}.\tag{2}$$

Here s is the moist entropy and the subscripts b and m refer to boundary layer and midtropospheric pressure levels, respectively (950 and 600 hPa in this paper); s_s^* is the moist entropy value a parcel has when saturated at the surface pressure and SST. When quasi-equilibrium assumptions hold, the boundary layer entropy is tethered via a moist adiabat to the saturation entropy throughout the free troposphere, and thus $s_b \approx s_m^*$. Under these conditions, the numerator of (2) can be regarded as a measure of the saturation deficit of the midtroposphere $(s_b - s_m \approx s_m^* - s_m)$ and hence is related to midcolumn dryness.

Luo et al. (2020) compared MERRA-2 and ERA-Interim SST and atmospheric temperature and humidity profiles over the Atlantic to in situ measurements taken during a field campaign. They found that differences between these reanalyses and observations were small (generally skin temperatures differed on the order of 0.1 K, lower-tropospheric temperature profiles remained within 2 K of the sounding, and relative humidity discrepancies were smaller than 10%). Nevertheless, subtle differences in measurements can affect the numeric values of the environmental parameters discussed above, particularly χ , which is a highly nonlinear metric strongly sensitive to humidity and temperature values. Luo et al. (2020) showed that boundary layer relative humidity in reanalyses generally agrees well with the variations measured by radiosondes (cf. their Fig. 11), but that MERRA-2 had slightly lower relative humidity values than ERA-Interim adjacent to the surface (cf. their Fig. 15); ERA-Interim was often drier than MERRA-2 above 950 hPa when boundary layers were deep (cf. their Fig. 15). We found that there are significant differences in the values (not trends) of χ computed in ERA5 and MERRA-2 if s_b were calculated from a single level such as 925 or 975 hPa to represent the boundary layer value. However, in both of these datasets using data from 950 hPa to calculate s_b best agreed with the values of s_b obtained by integrating all available levels between 1000 and 900 hPa. The differences in values of χ between the two datasets were also smallest when computed using 950-hPa data. For these reasons, we calculate s_b using 950-hPa data in this paper.

2) COMBINED INDICES

The thermodynamic and VWS parameters outlined in the last subsection can be combined into genesis indices, and a substantial amount of prior work has investigated the performance of particular combinations. Our primary purpose here is to analyze how the individual environmental factors vary during the early and late season, but a few of these combined metrics are useful as summary metrics. Emanuel and Nolan (2004) proposed an update of Gray's (1975) genesis index by combining PI, VWS, absolute vorticity, and relative humidity. Emanuel (2010) argued that χ given by (2) was preferable to relative humidity for studies of involving changes in climate, and Tippett et al. (2011) showed that absolute vorticity should be considered only at very low latitudes (i.e., absolute vorticity values poleward of ~15° latitude do not constitute a rate limiting factor for TC formation). Bruyère et al. (2012) showed that, at least in the Atlantic, good relationships between TC activity and a simplified index using only PI and VWS can be obtained; their formula, defined as a cyclone genesis index (CGI), is given by

$$CGI = \left(\frac{PI}{70}\right)^{3} [1 + 0.1(VWS)]^{-2}.$$
 (3)

Bruyère et al. (2012) argued that including relative humidity did not significantly augment the CGI, but variations in relative and even absolute humidity levels during the short period on which these indices are trained are small compared to potential changes in absolute humidity under larger climate change. Tang and Emanuel (2012) showed that ventilation, which is the product of the strength of the VWS with measures of midtropospheric dryness, can be measured using a ventilation index Λ that is a useful predictor of environments that support rapid intensification. This index is a nondimensional ratio defined by

$$\Lambda = \frac{\chi \times \text{VWS}}{\text{PI}} \tag{4}$$

and it relates the strength of ventilation to the strength of surface fluxes that supply moisture to the convection. We use (3) and (4) as ways of summarizing changes in the large-scale environment. The ventilation index (4) incorporates the additional effects from changing temperature and humidity levels that are potentially important under climate change (cf. Emanuel et al. 2008). However, Bruyère et al. (2012) showed that the simpler index given by (3) captures the interannual variability of Atlantic activity effectively during the period of historical observations. Given the sensitivity of χ to the source of data and to the levels used to calculate it, we urge caution in interpreting differences in trends between (3) and (4).

3. Changes in environmental conditions

In this section we discuss changes in the length of the season with favorable environmental conditions, with primary foci on

the early and late months of the Atlantic TC season. We calculate TC environmental factors using both ERA5 and MERRA-2 data, as discussed in section 2a. The storm season has grown longer over the North Atlantic during the last 40 years (Kossin 2008; Karloski and Evans 2016), and the data in Fig. 1 show that there are especially prominent changes during the early months of the season. The median date of the first named storm in the 1980s was 24 July, but this shifted to 27 May during the 2010s (as noted earlier, we begin our year on 1 March, so the January 2016 storm is considered to be a part of the 2015 season). Similarly, the median date of the 10th percentile of storm days shifted from 8 August in the 1980s to 16 July in the 2010s. If one fit a linear trend to this 40-yr period, the date of first TC genesis is moving 1.38 days yr^{-1} earlier (trend significance: p= 0.01), and the date of the 10th percentile of storm days shifts $0.57 \text{ days yr}^{-1} \text{ earlier } (p = 0.10).$ There are no significant movements in the last date of storm activity (the median is 16 November during the 1980s and 6 November during the 2010s) or in the 90th percentile of storm days (24 October is the median during both the 1980s and the 2010s), but there is an increase in the total number of storm days in all months of the storm season, including the late ones during autumn.

To aid our analysis and discussion, in addition to examining changes in the entirety of the North Atlantic basin, we examine the responses in three subregions defined by boundaries listed in Table 1 to isolate effects of changes in subtropical and midlatitude parts of the basin from those that occur in the tropical main development region. Approximately 80% of all geneses occurs in one of these three areas, and the trends to an earlier start to the season are evident for each of these subregions as well (see Table 1).

a. Early season (May-July) climatology

Given that activity during the early months of the season has increased over the past 40 years, we investigate how environmental conditions that favor TC development have changed in different parts of the Atlantic basin during these months. We begin with an analysis of the 40-yr mean of May-July values of the TC environmental parameters discussed in section 2 using both ERA5 and MERRA-2 datasets. We choose this 3-month period to define the early (and preseason) months based on data shown in Fig. 1: by the end of July in most years, the Atlantic has already experienced 10% of that season's storm days (Fig. 1a), and the first occurrence of genesis has not infrequently occurred during May (Fig. 1a). We isolate these months from the much more active months of August-October (Figs. 1c,d) to assess whether environmental conditions have also become more conducive during the beginning part of the season.

The left column of Fig. 2 shows 1980–2019 mean climatological values of May–July (MJJ) averages of PI (Fig. 2a), VWS (Fig. 2c), and the CGI (Fig. 2e) calculated using daily ERA5 data. Panels on the right side of Fig. 2 show the difference in 1980–2019 MJJ climatological values between MERRA-2 and ERA5. Locations where the difference between ERA5 and MERRA-2 MJJ climatological means are

TABLE 1. Definitions of three subregions of the North Atlantic (NA) basin used in this paper, median dates for the 1st, 10th, 90th, and 99th percentiles of storm days (SD) in each region over the period 1980–2019, and trends over the 1980–2019 period for the 1st, 10th, 90th, and 99th percentiles of storm days in each subregion. The p value for each trend is given in the parentheses, and data in boldface highlight significant trends (assessed at confidence interval of p < 0.10).

Subregions	Tropical North Atlantic (TNA)	Gulf of Mexico (GOM)	Western subtropical North Atlantic (WSNA)
Latitude range	8°–20°N	18°-30°N	20°-40°N
Longitude range	65° – 20° W	$100^{\circ} - 80^{\circ} W$	$80^{\circ}-60^{\circ}W$
1st SD			
Median	8 Aug	30 Jun	5 Jul
Trend (p)	-6.67 (0.04)	-10.61 (0.06)	-10.09 (0.09)
10th SD			
Median	15 Aug	16 Jul	3 Aug
Trend (p)	-4.40 (0.12)	-13.19 (0.01)	-10.59 (0.05)
90th SD			
Median	22 Sep	6 Oct	4 Oct
Trend (p)	3.48 (0.12)	-8.23(0.12)	3.89 (0.20)
99th SD	, ,	. ,	` '
Median	27 Sep	9 Oct	19 Oct
Trend (p)	5.37 (0.46)	-4.79 (0.27)	4.46 (0.36)

statistically significant (at 99% confidence level) are marked with a gray cross in the right panels.

There are some notable differences in the mean climatological values between ERA5 and MERRA-2. As seen in Fig. 2b, PI is higher in ERA5 than in MERRA-2, and this is driven primarily by larger near-surface humidity levels and slightly warmer lower-tropospheric temperatures in ERA5 than in MERRA-2 [cf. Luo et al. (2020), who found similar differences between ERA-Interim and MERRA-2]. To test whether the increased vertical resolution of ERA5 also affected the PI values, we recalculated ERA5 PI using only the subset of pressure levels contained in MERRA-2 (ERA5 contains additional data at 225, 175, and 125 hPa, while MERRA-2 has an additional level of data at 725 hPa). We found that ERA5 PI remained larger than MERRA-2 PI, but that differences in PI values with and without the uppertropospheric levels were generally no larger than 1 m s⁻¹. This suggests the PI differences seen in Fig. 2b are primarily attributable to differences in boundary layer temperature and humidity between the datasets, with a smaller, secondary contribution from different near-tropopause vertical resolution. The differences in VWS (Fig. 2d) between datasets are small (less than 1 m s⁻¹) compared to mean values and are not statistically significant across all of the NA basin. CGI values during MJJ are large in the Gulf of Mexico (GOM) and the southern half of the western subtropical North Atlantic (WSNA) (Fig. 2e), but differences between the datasets here are small and insignificant. There are also large values of CGI during MJJ in the southwestern part of the TNA and these values are significantly lower in MERRA-2 than in ERA5 owing to the lower PI and higher VWS in that dataset found here.

Figure 3 shows the 1980–2019 MJJ climatology for χ given by (2) (top row), its numerator, which is proportional to the entropy deficit (ED) of the middle troposphere (second row), its denominator, which is proportional to the strength of the surface fluxes (SF) (third row), and the logarithm of the ventilation index Λ given by (4) (bottom row). The left

panels use daily data from ERA5, while the right panels show the differences in values when data from MERRA-2 are used.

Values of χ are lower (i.e., more favorable) in the GOM and WSNA than in the TNA during MJJ. The numerator, which is proportional to midtropospheric entropy deficits, is smaller in the eastern GOM and in the WSNA than in the TNA, indicating that a smaller amount of water vapor is needed to saturate the middle troposphere here. The denominator of (2), which is proportional to the strength of the surface entropy fluxes, is highest in the GOM, the southern part of the WSNA, and along the Gulf Stream near the southeast coastline of the United States. The high values of SF near the U.S. coastline in MJJ are slightly smaller when calculated using ERA5 data compared to calculations with MERRA-2. Here MERRA-2 features drier air in the boundary layer, leading to larger thermodynamic disequilibrium; the difference in SST between ERA5 and MERRA-2 is negligible here (not shown). Figures 3d and 3f show statistically significant differences in values of both ED and SF over the Caribbean Sea between the two datasets. Temperatures here at 600 hPa are warmer in MERRA-2 than in ERA5, but they are lower at 950 hPa than in ERA5; MERRA-2 also has higher 950-hPa humidity. As we noted in section 2c(1), the numeric values of χ are quite sensitive to the vertical level used to compute its boundary layer entropies. We chose 950 hPa here as using data from that level most closely estimated values vertically integrated over the 1000-900-hPa layer as well as minimized the difference between ERA5 and MERRA-2.

Given the smaller SF values in ERA5 in the Gulf of Mexico and western subtropical North Atlantic to the east of the U.S. coastline, χ is smaller in MERRA-2 than in ERA5 (Fig. 3b). While combined metrics like CGI and the ventilation index show different numerical values between the datasets (Figs. 2f and 3h, respectively), the differences are generally not statistically significant. The exception to this is an area in the tropical North Atlantic (TNA) immediately east of the Lesser

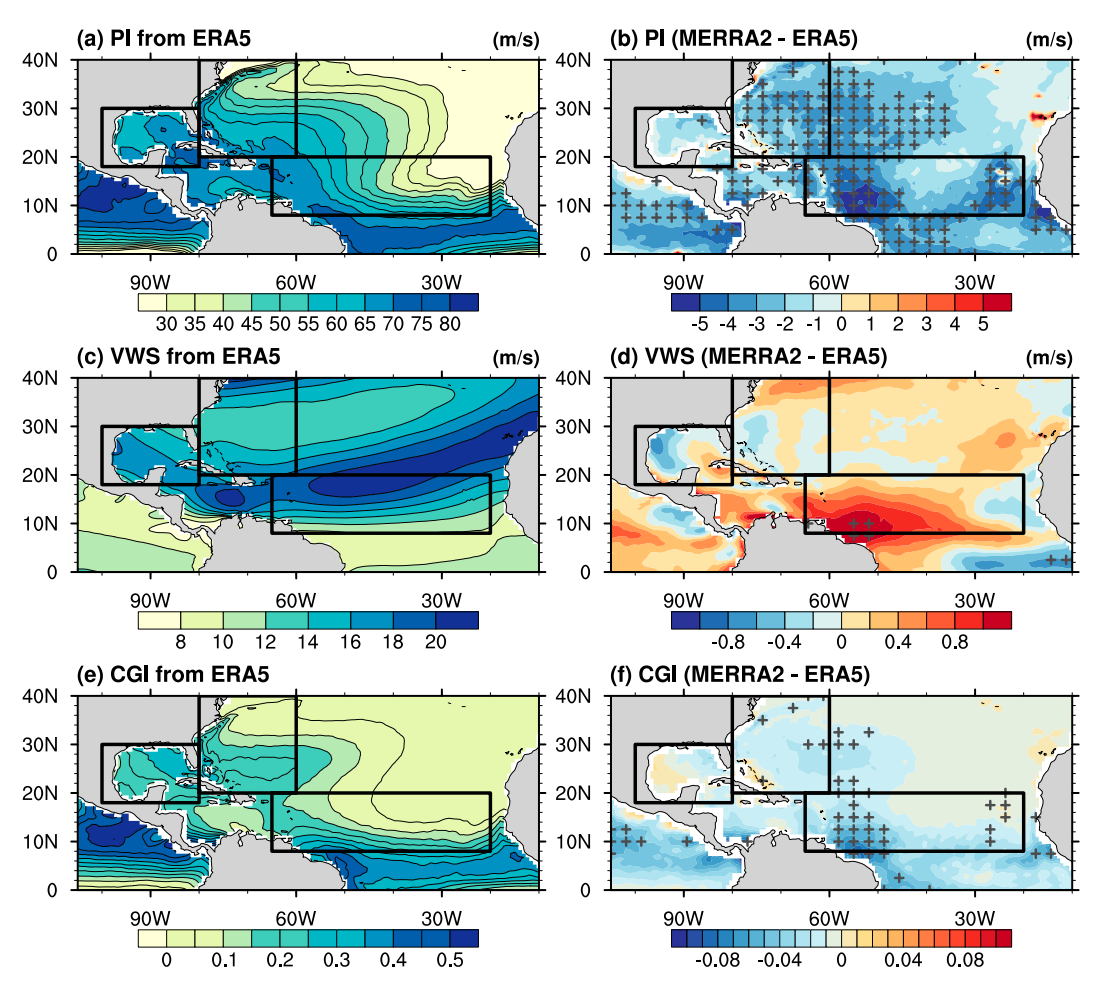


FIG. 2. (left) May–July (MJJ) mean in environmental genesis factors over the NA from1980 to 2019 using ERA5 and (right) the difference between MERRA-2 and ERA5. (a) Potential intensity (PI; in m s⁻¹) in ERA5 and (b) the difference between MERRA-2 and ERA5. (c) Vertical wind shear between the 250- and 850-hPa levels (VWS; in m s⁻¹). (d) As in (b), but for VWS. (e) MJJ mean cyclone genesis index (CGI) in ERA5. (f) As in (b), but for CGI. The black rectangles in each panel show the subregions of the NA discussed in the text. Gray crosses in the panels of the right column show grid points with a statistically significant difference (at 99% confidence) between ERA5 and MERRA-2 data.

Antilles, where the differences in PI between datasets is enough to drive CGI to statistically significantly higher values in ERA5 than in MERRA-2. We take from all of these comparisons evidence that the numeric values of these parameters are sensitive to subtle differences in humidity and thermal profiles as well as to vertical resolution of datasets. Despite these differences, we show below there are trends in some fields common to both datasets.

b. Changes from 1980 to 2019

Figure 4 shows trends in the MJJ values of environmental factors over the 40-yr period from 1980 to 2019 in both ERA5 (left column) and MERRA-2 (right column). Significance was assessed using a Mann–Kendall test with a 90% confidence level; this test assumes that data are independent (from one year to another) but does not presume that trends, if present, are linear.

PI shows sharp and statistically significant increases in the GOM, WSNA, and in the western part of the TNA (i.e., east of the Lesser Antilles). This increase in PI from 1980 to 2019 is significant in both ERA5 and in MERRA-2 [although the absolute values of PI differ between the datasets (Fig. 2b), the upward trend is common to both]. Figure 5 shows that in both the GOM and in the WSNA, the area covered by high values of PI (i.e., PI > 55 m s⁻¹)¹ becomes more extensive during May–July as time progresses from the 1980s to 2010s, with statistically significant increases in the fraction of each area covered by high PI values in the early parts of the season. This

 $^{^{1}}$ PI obtains large values only where deep convection is possible. See, for example, the discussion in section 3 of Korty et al. (2012b), which shows that values of PI > 55 m s⁻¹ are obtained only when the equilibrium level (or level of neutral buoyancy) is found in the upper troposphere.

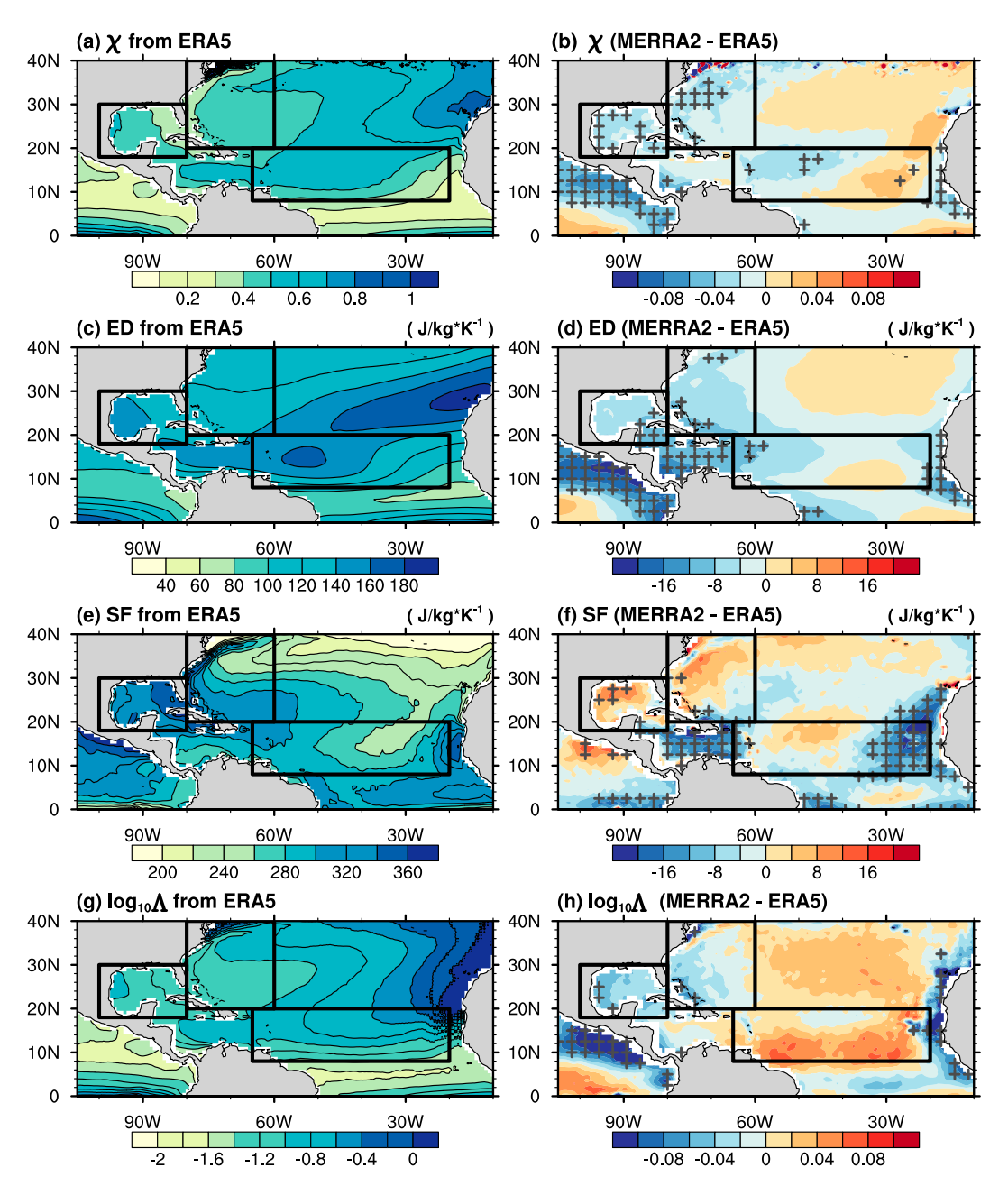


FIG. 3. May–July (MJJ) climatological mean from 1980 to 2019 of (a) χ computed with ERA5 data. (b) Difference in MJJ χ climatological means computed with MERRA-2 and ERA5 data. (c) The MJJ climatological mean (1980–2019) of the numerator of χ , which is proportional to midtropospheric entropy deficits (ED), using ERA5 data. (d) As in (b), but for ED. (e) MJJ climatological mean (1980–2019) of the denominator of χ , which is proportional to surface fluxes of entropy (SF) using ERA5 data. (f) As in (b), but for SF. (g) Base-10 logarithm of the MJJ (1980–2019 mean) ventilation index Λ using ERA5 data. (h) As in (b), but for $\log_{10}\Lambda$.

trend to more extensive spatial coverage continues through the heart of the season in the WSNA; the GOM features nearly universal coverage of high PI from July to early October throughout the entire 40-yr period. In the TNA, the increase in PI values seen in the areas immediately to the east of the Lesser Antilles in MJJ (Figs. 4a,b) occurs where PI is already large; the

areal coverage of high PI in this region does not show statistically significant increases until the main part of the season. Both the GOM and WSNA also show statistically significant increases in high PI during the late part of the season, showing that the length of the season with a large amount of territory supporting high PI has grown in these regions over the past

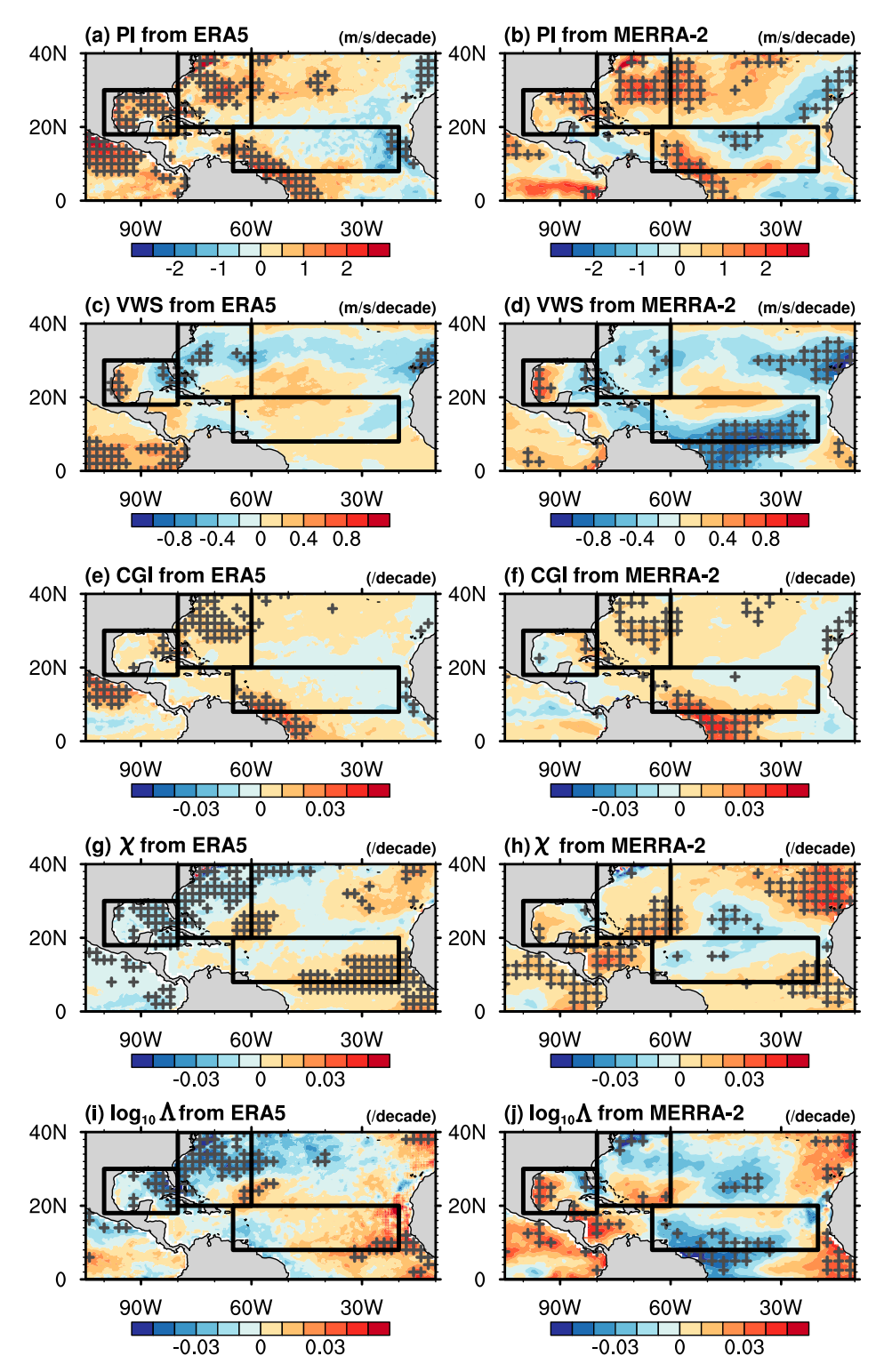


FIG. 4. The trend in May–July (MJJ) values of environmental factors from 1980 to 2019. Values using ERA5 data and (right) MERRA-2. (a),(b) Trends in PI (in m s⁻¹ decade⁻¹). (c),(d) Trends in VWS (in m s⁻¹ decade⁻¹). (e),(f) Trends in CGI. (g),(h) Trends in χ . (i),(j) Trends in the base-10 logarithm of ventilation index (log₁₀ Δ). Units in (e)–(j) are change in value per decade. Points where trends are statistically significant (p < 0.10) are marked with gray crosses.

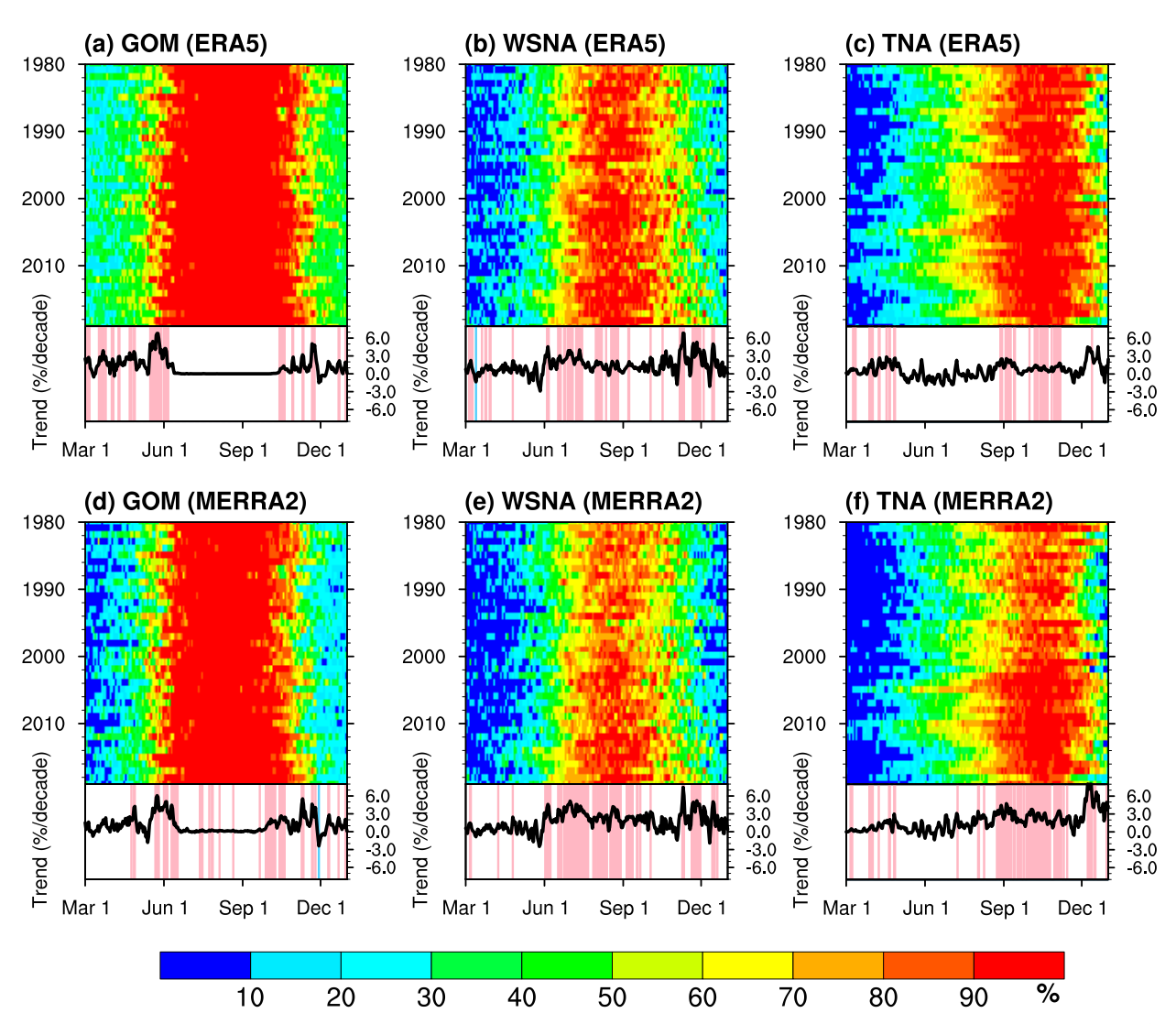


FIG. 5. Hovmöller diagrams for the fraction of (a),(d) the GOM, (b),(e) the WSNA, and (c),(f) the TNA covered by PI > 55 m s⁻¹ from 1 Mar to 31 Dec each year. Data from (top) ERA5 and (bottom) MERRA-2. The black curves below each Hovmöller diagram show trends for each day of the year in areal coverage, with statistically significant (p < 0.10) positive trends shown in pink. (There are no statistically significant negative trends in coverage.) Units in each panel are the percentage of the subregion with PI > 55 m s⁻¹, and the units of trends are % decade⁻¹.

40 years. Areal coverage of high PI also increases from 1980 to 2019 during the peak months of the season in the WSNA.

Figure 6 shows these changes in a slightly different way: the percentage of each region (left: GOM; right: WSNA) with PI exceeding the value shown on the *y* axis is plotted over the course of the season in the 1980s (top) and again for the 2010s (middle), with the difference between them shown in the bottom row. Territorial coverage of high PI not only expands to earlier and later in the year, but the probability of finding high values of PI in each month of the season increases also (the curves not only expand left and right but also move up). Figure 6 was constructed using data from ERA5, but the behavior is qualitatively similar using MERRA-2 data (not shown).

While mean values of PI increase and the percentage of time and space covered by high values of PI also increase from

1980 to 2019, VWS shows small but statistically significant changes during MJJ in parts of the GOM (Fig. 4c). VWS shows a statistically significant increase (a condition that is less favorable) in the western GOM during MJJ but a statistically significant decline (a favorable change) in the vicinity of Florida in both datasets (Figs. 4c,d). The low values found in the southern TNA (Figs. 2c,d) show a further significant decline in MERRA-2 (Fig. 4d), but there is no significant change in ERA5 (Fig. 4c). Across much of the basin, there are only small (i.e., changes less than 0.5 m s⁻¹ decade⁻¹) and statistically insignificant changes over the period. When combined with PI, these changes lead to increases in MJJ CGI near Florida, in much of the WSNA, and in the western TNA nearest the Lesser Antilles in both ERA5 and MERRA-2 (Figs. 4e,f).

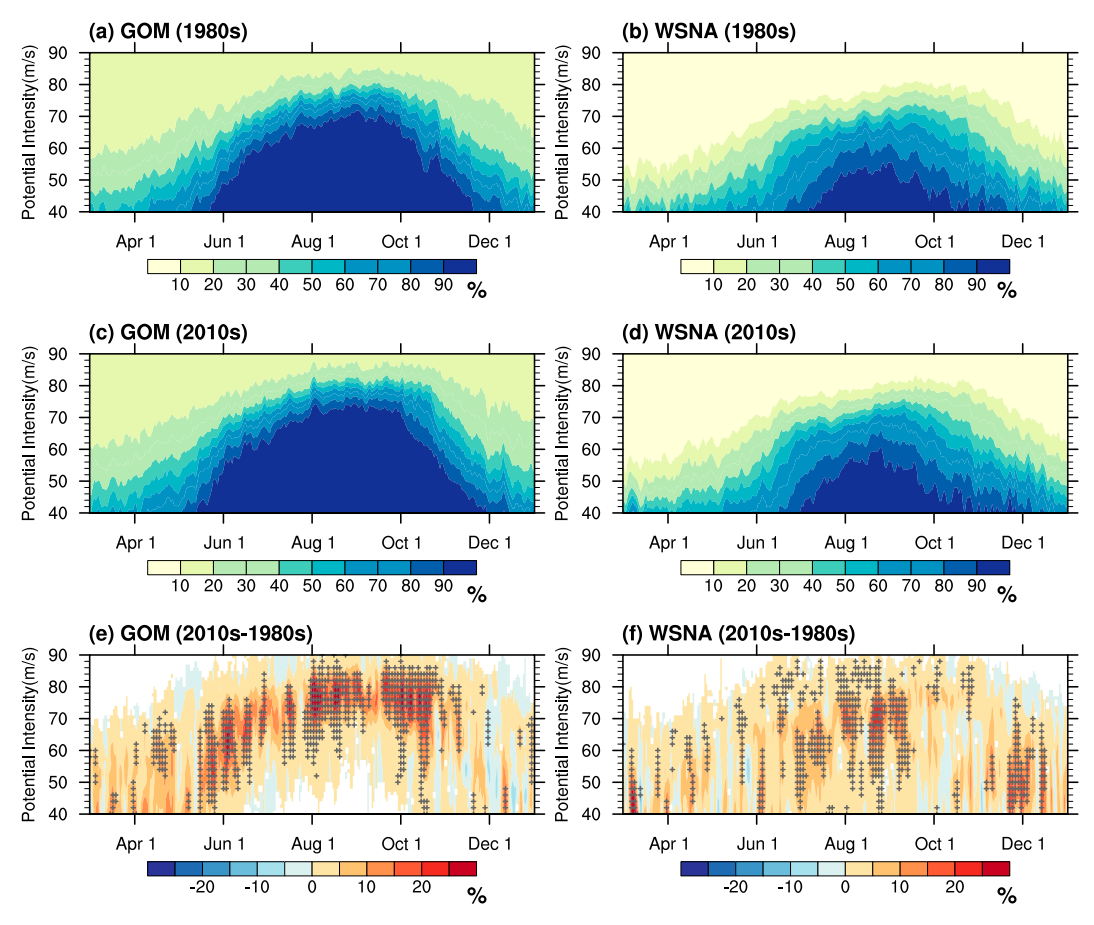


FIG. 6. (a) The percentage of the area of the GOM having PI exceeding the value shown on the y axis as a function of day of the year during 1980–89 computed using ERA5 data. (b) As in (a), but for the WSNA. (c) As in (a), but for the 2010–19. (d) As in (b), but for 2010–19. (e) Difference in coverage of the GOM between the 2010s and 1980s with statistically significant differences (at 90% confidence) marked by black crosses. (f) As in (e), but for WSNA.

As we mentioned earlier, calculations of χ turn out to be quite sensitive to the differences in temperature and humidity values between ERA5 and MERRA-2, and these discrepancies can lead to different trends when calculated with ERA5 or MERRA-2. There is a statistically significant decrease in MJJ climatological values of χ (i.e., this parameter becomes more favorable with time) over the GOM and northern part of the WSNA in ERA5 (Fig. 4g), but there are no significant trends here in MERRA-2 (Fig. 4h). The southeastern part of WSNA shows a statistically significant increase in χ (i.e., becomes less favorable with time) in both MERRA-2 and ERA5. Among the reasons for the differences in trends in the GOM and WSNA are subtle differences in humidity levels between ERA5 and MERRA-2: over the GOM and WSNA, MERRA-2 relative humidity levels at 600 hPa are higher during MJJ than in ERA5 in the 1980s and 1990s, but the differences between datasets diminish from the early 2000s onward. Conversely, relative humidity levels at 950 hPa are larger in ERA5 than in MERRA-2 over GOM and WSNA during MJJ in the 1980s and 1990s, with differences between datasets again diminishing after about 2000. The numeric value of χ is sensitive to these differences in data, and they

are substantial enough to have consequences for trends in combined metrics like the ventilation index (Figs. 4i,j). In ERA5, the ventilation index decreases (becomes more favorable) near Florida and in much of the WSNA, consistent with the increases in CGI (it also becomes more favorable). But using data from MERRA-2, the ventilation index shows no significant differences over most of the WSNA, although it does show consistency with changes in CGI (i.e., both trends to more favorable MJJ conditions) in the small area surrounding Florida. There is qualitative agreement in both ERA5 and MERRA-2 that PI and CGI increase near Florida and the U.S. Atlantic coastline. The ventilation index also becomes more favorable during the early season here in ERA5, but the discrepancy in how (4) changes with MERRA-2 data underscores its sensitivity to subtle differences in calculation.

c. Changes in coverage of favorable conditions across the North Atlantic basin

In this section, we consider changes in environmental parameters across all of the North Atlantic (the three subregions discussed extensively in prior sections, plus the Caribbean Sea) and throughout the entire length of the TC season. The

number of storm days (Fig. 1d) has increased in recent decades, and there are statistically significant increases from 1980 to 2019 during the months of July, September, and October. We focus here on the parameters that demonstrate trends from 1980 to 2019 during at least some part of the season, and we note that most of those documented below are seen in both ERA5 and MERRA-2 (although discussion of any discrepancies between datasets is noted, where they occur). As noted earlier, the most prominent differences between datasets often arise in time series of χ or in those of parameters involving it (e.g., the ventilation index).

To assess whether the frequency of favorable conditions in any given environmental factor is changing, we define thresholds for favorability based on results from prior studies (Korty et al. 2012b; Tang and Emanuel 2012; Bruyère et al. 2012; Tang and Camargo 2014; Rios-Berrios and Torn 2017). Our results are qualitatively similar if thresholds are varied slightly from values used here. We define favorable VWS when its daily value is less than 10 m s⁻¹; favorable PI is defined as larger than 55 m s⁻¹ (Korty et al. 2012b); favorable values of χ are those less than 0.5; favorable CGI is larger than 0.3; and the ventilation index is defined to be favorable if the base-10 logarithm of its value is less than -1.4. Because χ is a meaningful quantity only if deep convection is possible, we place an additional constraint on its definition of favorability: for χ to be labeled favorable, not only must $\chi < 0.5$ but the level of neutral buoyancy (LNB) from the PI algorithm on that day and at that location must also have a pressure less than 500 hPa (i.e., convection must be able to reach the upper troposphere).

Figure 7 shows Hovmöller diagrams for the fraction of the entire NA basin with favorable values each day from 1980 to 2019 for each environmental factor. There is an increase in coverage of low VWS during the early and late part of the seasons (also see Figs. 4c and 4d for trends in MJJ mean). There is no coherent shift in the coverage of low χ ; this parameter will increase with warming if relative humidity does not also rise, and its sensitivity to variations in how it is calculated and to subtle differences in data was noted earlier. The major shift occurs in PI, and in both ERA5 and in MERRA-2 high PI covers larger amounts of the basin as time progresses forward over the 40 years analyzed. These changes are statistically significant over large parts of the season, especially during the peak months from August into autumn.

Figure 8 shows that the increase in coverage of high PI and of low VWS lead the coverage of high values of CGI to increase during the early and late parts of the season. (Figure 8 shows data computed from ERA5, but this pattern of statistically significant increases in the early and especially late part of the seasons is also evident using MERRA-2.) The GOM and WSNA show increases in coverage of high CGI early and late in the season, but the largest change occurs in the TNA. Here the areal extent of high CGI is much larger after 2000 during June and from September to November than as the case in the late twentieth century. This is consistent with the significant increase in coverage of high PI coupled with an increase in coverage of low VWS. There is an increase in the

length of the season with low ventilation index also (not shown), but the changes are less prominent than CGI as it depends on PI less strongly than CGI and is also affected by variations in χ .

Figure 9 summarizes the trends from 1980 to 2019 in each of the environmental parameters. To facilitate discussion, we break the season into three periods: early [May-July MJJ)], middle [August-October (ASO), the most active months of the season; cf. Figs. 1c,d), and late [November and December (ND)]. We tabulate the number of days with favorable values for each parameter (defined using the same thresholds used in Figs. 7 and 8) at each grid point, and these tabulations are then spatially averaged for separately for each region (GOM, WSNA, or TNA) as well as for the entire NA basin (GOM, TNA, WSNA, and Caribbean Sea together). Trends from 1980 to 2019 within early, middle, and late months of the season are assessed for each parameter (calculated with ERA5 data and repeated using MERRA-2 data). Positive trends (colored with yellow, orange, or red in Fig. 9) represent an increase in the number of days with favorable values of a particular parameter (i.e., large values of PI or CGI, small values of VWS, χ , or Λ), and negative trends (colored with blue or purple in Fig. 9) represent a decrease in the number of days with favorable values. Nearly all of the statistically significant trends that are common to both ERA5 and MERRA-2 are positive (i.e., an increasing number of days featuring favorable conditions).

Across the entire NA basin (Fig. 9, top row), the number of days with favorable PI increases in all months of the year, and the rise is statistically significant in both datasets during the middle and late months of the season; the rise is also statistically significant during MJJ in the MERRA-2 dataset. When averaged across the full basin, the number of days favorable CGI undergoes a statistically significant increase during the middle and late months of the season, driven primarily by the increase in PI. There is an increase in the number of days with low χ and Λ during ASO and ND, but the trend is significant only when calculated using ERA5 during ASO. In the TNA, the number of days with favorable values of most parameters increases during ASO, and the trends in PI and CGI are statistically significant in both datasets. There are statistically significant increases in the number of days with high PI in the GOM during MJJ and ASO in both ERA5 and MERRA-2, and the number of days with high PI grows in early, middle, and late months of the season in the WSNA (using data from ERA5 or MERRA-2).

In summary, we find that there is a statistically significant increase in the number of days with high values of PI in all parts of the basin and in most months of the season. There are increases early and middle months of the storm season in the GOM and WSNA, and in the TNA in the season's peak and autumn months. The number of days with high CGI increases across full basin in ASO and ND, as well as in TNA during ASO. Bruyère et al. (2012) argued that CGI captured the behavior of TCs in the North Atlantic during the last several decades, and that more complicated metrics incorporating measures of humidity may not be necessary in this basin. Although mostly statistically insignificant, note that there are

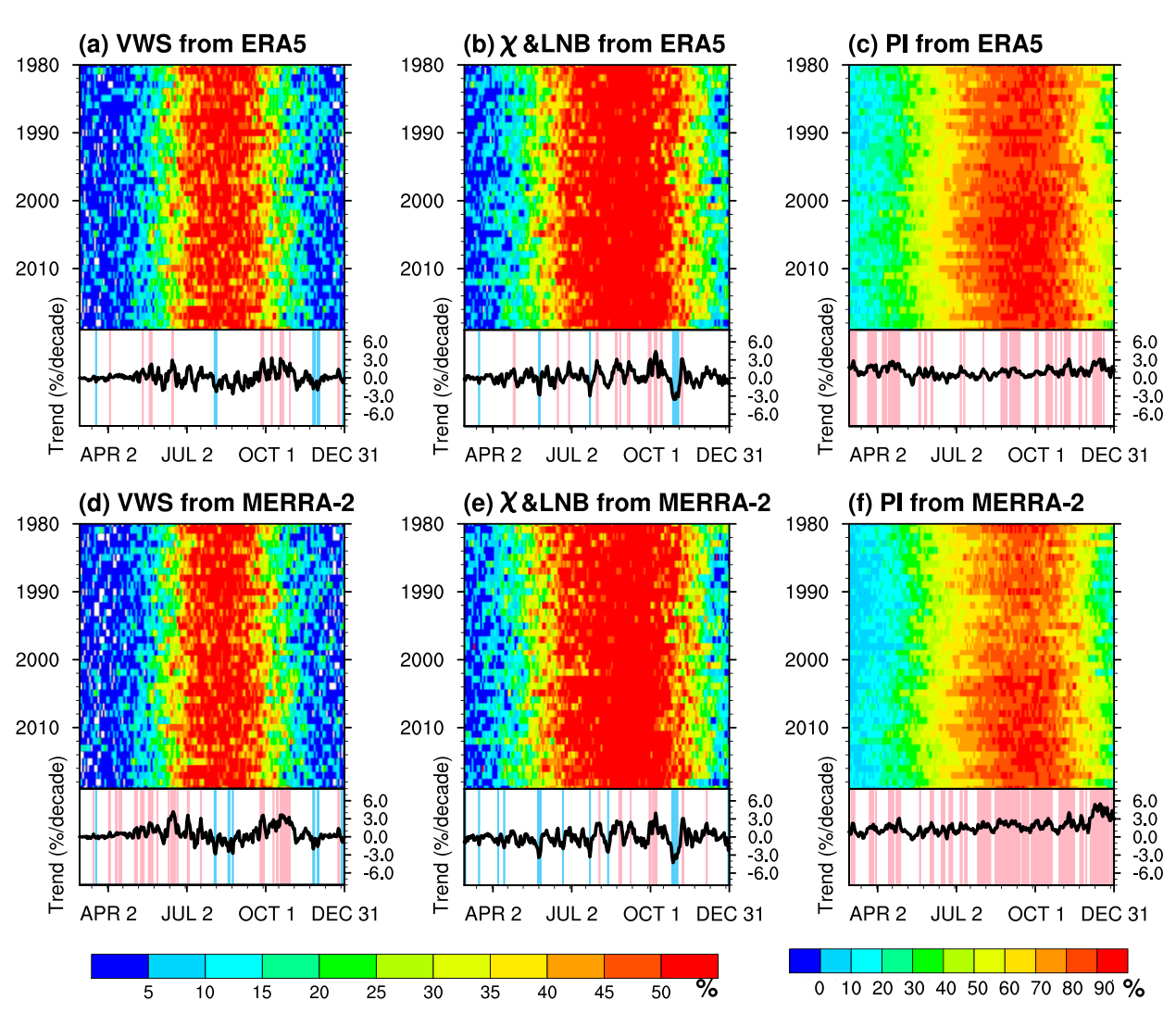


FIG. 7. (a) Hovmöller diagram of the fraction of the area of the NA basin VWS < 10 m s⁻¹ using ERA5 data. (b) As in (a), but the fraction of the NA basin with favorable values of χ (see text for details). (c) As in (a), but for fraction of the area with PI > 55 m s⁻¹. (d)–(f) As in (a)–(c), but constructed using MERRA-2 data. The black curves below each Hovmöller diagram are trends in daily values over the period 1980–2019; pink shadows highlight statistically significant (p < 0.10) positive trends, and blue shadows highlight statistically significant negative trends. Units in each Hovmöller diagram are percentage of NA basin with favorable conditions, and the units of each trend are % decade⁻¹.

differences in the sign of trends in χ and Λ in many of the subregions between ERA5 and MERRA-2, underscoring the need to pay close attention to the sensitivity of these parameters to the temperature and humidity data used to calculate them.

4. Changes to environmental conditions in a high-resolution projection

Future warming resulting from increase in carbon dioxide and other greenhouse gases has been shown to have the ability to alter many properties of the climatology of tropical cyclones (e.g., Sobel et al. 2016). Dwyer et al. (2015) showed that the North Atlantic season length for tropical cyclones downscaled

from projections in CMIP3 and CMIP5 increased over the course of the warming twenty-first century, but that direct simulations using a high-resolution atmospheric model (SST was prescribed) produced a shorter season. They also showed that a tropical cyclone genesis index (TCGI; Camargo et al. 2014) that includes saturation deficits as a predictor has a shorter season with high values under CMIP5 projections of warming (cf. their Fig. 7). Here we revisit these results to focus on the changes of individual environmental factors in different months of the season; we use a new high-resolution coupled simulation of projected changes using a CESM run contributed to the HighResMIP.

As introduced in section 2b, the simulation we analyze here was implemented following the protocols established for

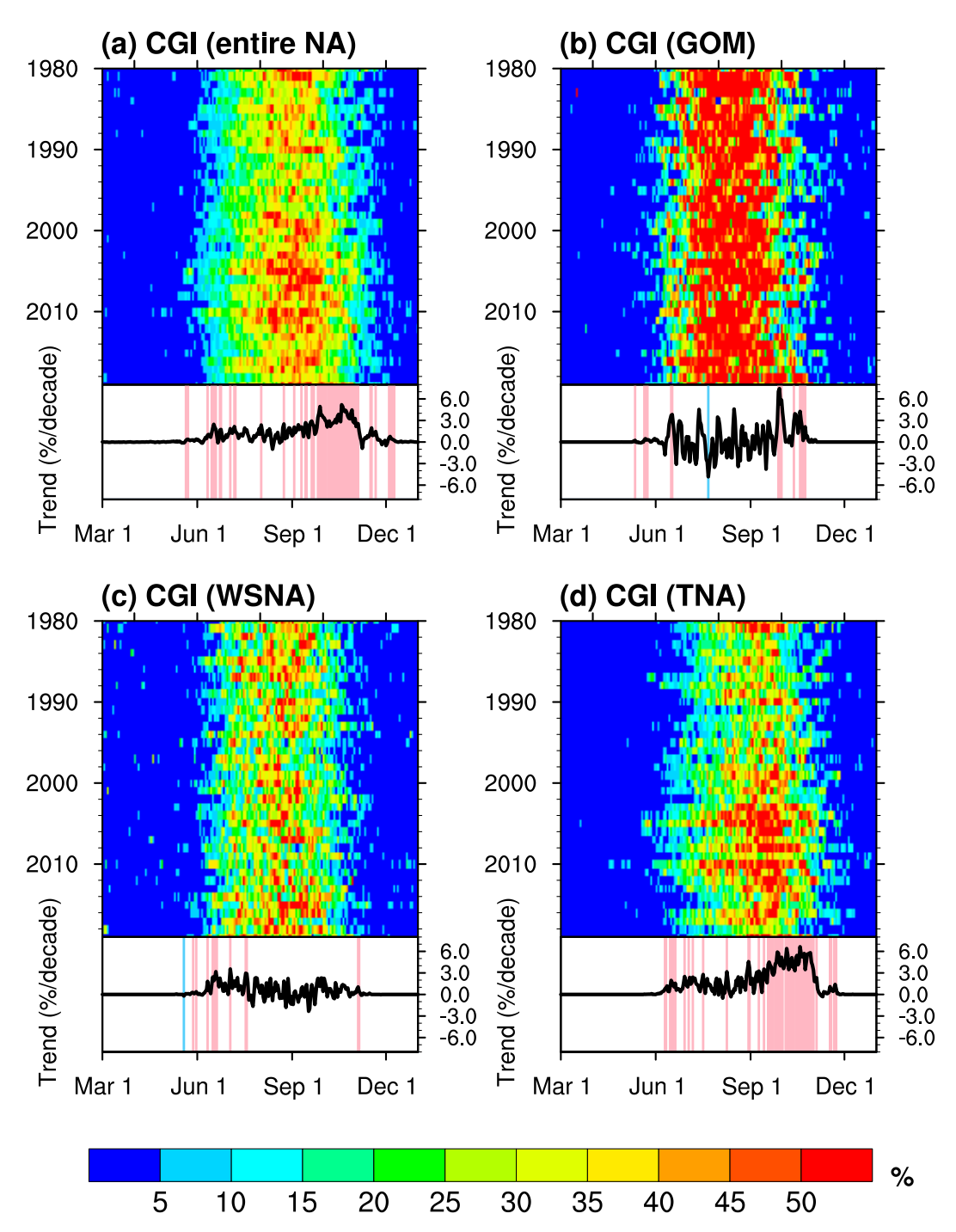


FIG. 8. (a) Hovmöller diagram of the fraction of the entire NA covered with CGI > 0.3 for each day of the season using ERA5 data. (b) As in (a), but for GOM only. (c) As in (b), but for WSNA. (d) As in (b), but for TNA. The black curves below each Hovmöller diagram show their trends, with statistically significant (p < 0.10) positive trends shown in pink and negative trends in blue. Units of each Hovmöller diagrams are percentage of area covered by favorable CGI values, and the units of trends are % decade⁻¹.

CMIP6 (Eyring et al. 2016) and data were output with a frequency to meet the requirements of the HighResMIP CMIP6 (Haarsma et al. 2016). A 130-yr coupled atmosphere-ocean-land-ice model simulation control simulation was

generated with perpetual 1950 greenhouse gas (GHG) emissions, and the coupled transient climate simulation analyzed here was initialized from the end of the control run. The transient run was forced by observed GHG emissions from 1950

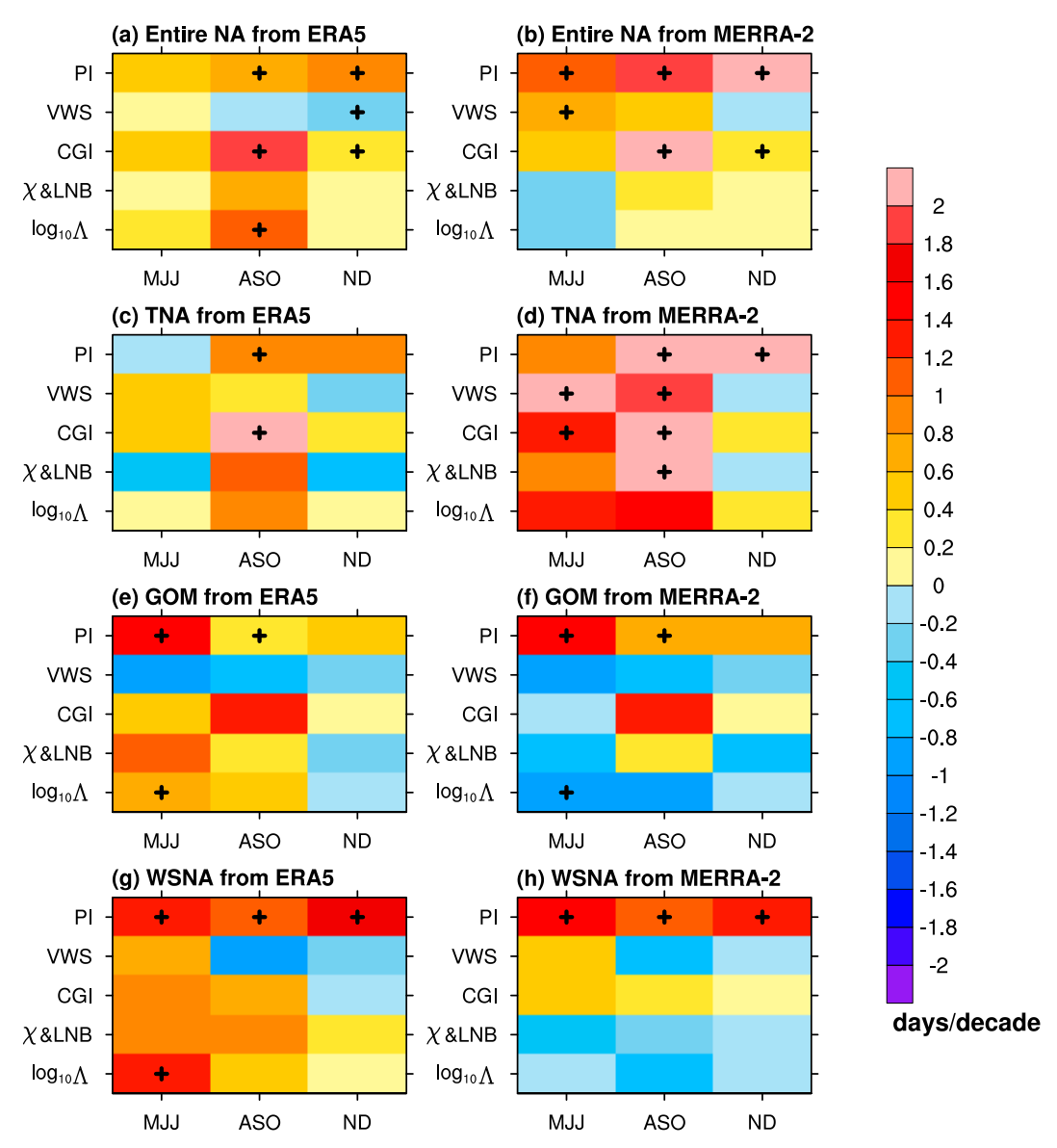


FIG. 9. (a) Trend in the number of days with favorable values of various environmental factors across the NA basin in the early (MJJ), middle [August–October (ASO)], and late months of the Atlantic TC season [November and December (ND)] using ERA5 data. Favorable values of each parameter are as defined in the text: PI > 55 m s⁻¹, VWS < 10 m s⁻¹, CGI > 0.3, χ < 0.5, and LNB < 500 hPa, and $\log_{10}\Lambda$ < -1.4. (b) As in (a), but using data from MERRA-2. (c),(d) As in (a) and (b), but for TNA. (e),(f) As in (a) and (b), but for GOM. (g),(h) As in (a) and (b), but for WSNA. Trends that are statistically significant (p < 0.10) are marked with a cross; units in all panels are number of days per decade.

to 2014 and then under GHG emissions projected in RCP8.5 from 2015 to 2100. We analyze two portions of this simulation: 1) the years that overlaps with those we analyzed using reanalysis data (1980–2019) and 2) the continued projections from 2020 to 2100. Note that the years that overlap with those of the reanalysis data are a mixture of those forced by historical emission levels (until 2014) and RCP8.5 projections (2015 forward). Averaged over 1980–2019, this simulation of CESM features surface and tropospheric mean temperatures slightly higher than observed in ERA5 or MERRA-2, but relative humidity over the GOM, WSNA, and TNA slightly lower than

in the reanalysis sets. The simulation has lower PI and VWS and higher χ in the Atlantic during 1980–2019 than was calculated using the reanalysis data.

Given these differences, an ensemble of model simulations would offer preferential advantages by averaging over different biases and deficiencies present in any one particular simulation. However, the volume of data we analyze here is considerably larger than what is customarily examined in studies of TC environmental factors: not only is there very high spatial resolution, but our calculations of these parameters are done with daily (rather than monthly) data. Given

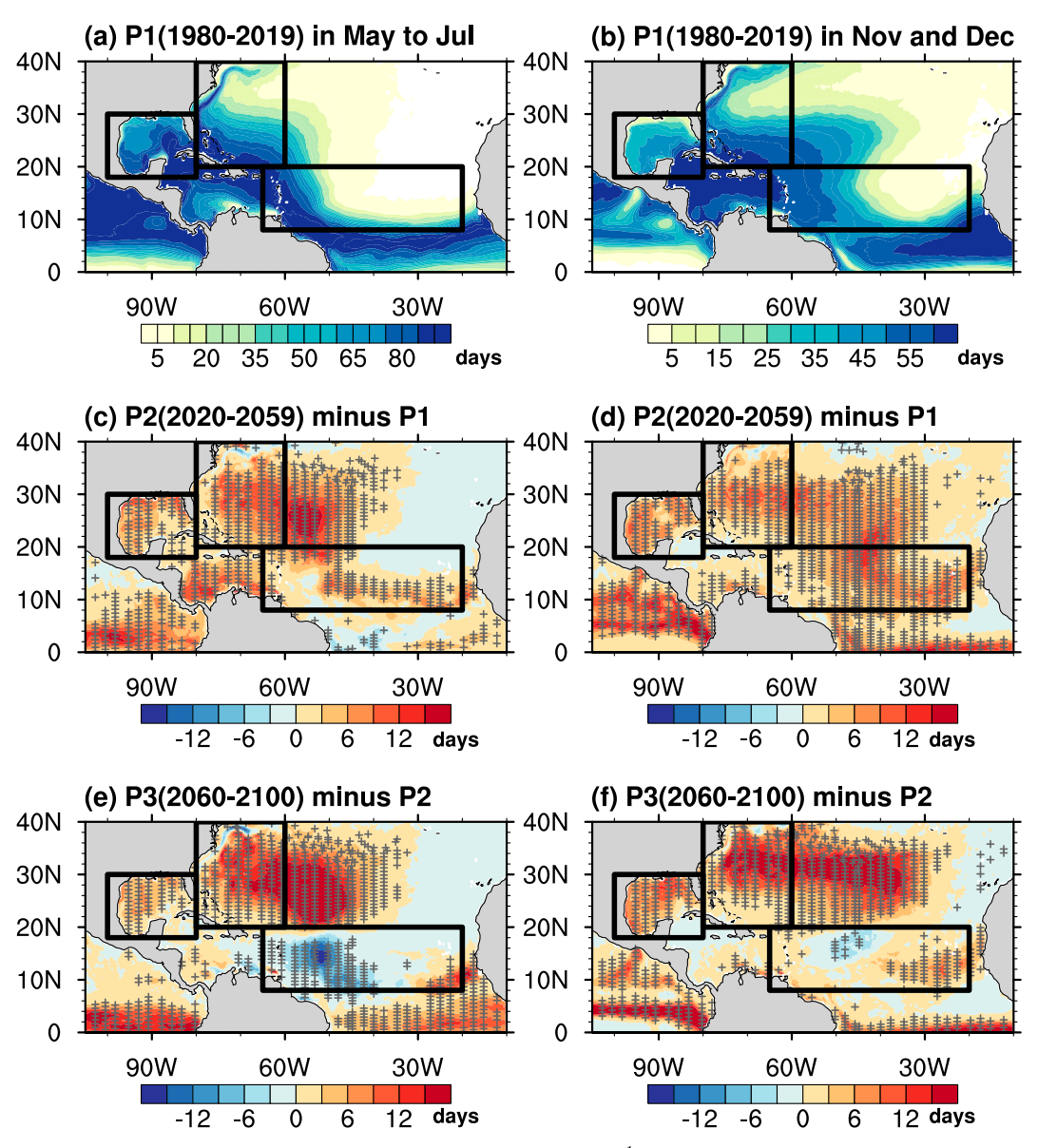


FIG. 10. (a) The average number of May–July days with PI $> 55 \text{ m s}^{-1}$ during the period 1980–2019. (b) The average number of November and December days with PI $> 55 \text{ m s}^{-1}$ during the period 1980–2019. (c) The change in the average number of May–July days with PI $> 55 \text{ m s}^{-1}$ during 2020–59 from the mean shown in (a) (1980–2019). (d) As in (c), but for November and December. (e) The change in the average number of May–July days with PI $> 55 \text{ m s}^{-1}$ during 2060–100 compared to 2020–59. (f) As in (e), but for November and December. Changes that are statistically significant (at 90% confidence interval) are marked with a gray cross. Units in all panels are number of days.

this very large amount of data, we choose to introduce our analysis of this single high-resolution simulation here in order to illustrate the type of comparisons that are becoming possible with high-resolution simulations, but we encourage readers to bear in mind that future work will need to be done to assess the robustness of these particular comparisons. Nevertheless, we document noteworthy trends in PI that appear prominently both in the reanalysis data examined in section 3 and the projections in this simulation presented below.

The top row of Fig. 10 shows the number of days (averaged over years 1980–2019) with PI $> 55 \text{ m s}^{-1}$ in the simulation during the early months of the season (left column) and in the late part of the season (right column) across the North Atlantic. The middle row shows how the number of days with high PI changes in the projection of the next four decades: there is a statistically significant increase in the number of days with high PI during both the early and late parts of the season across much of the subtropics. The bottom row shows that this pattern continues into the last four decades of the twenty-

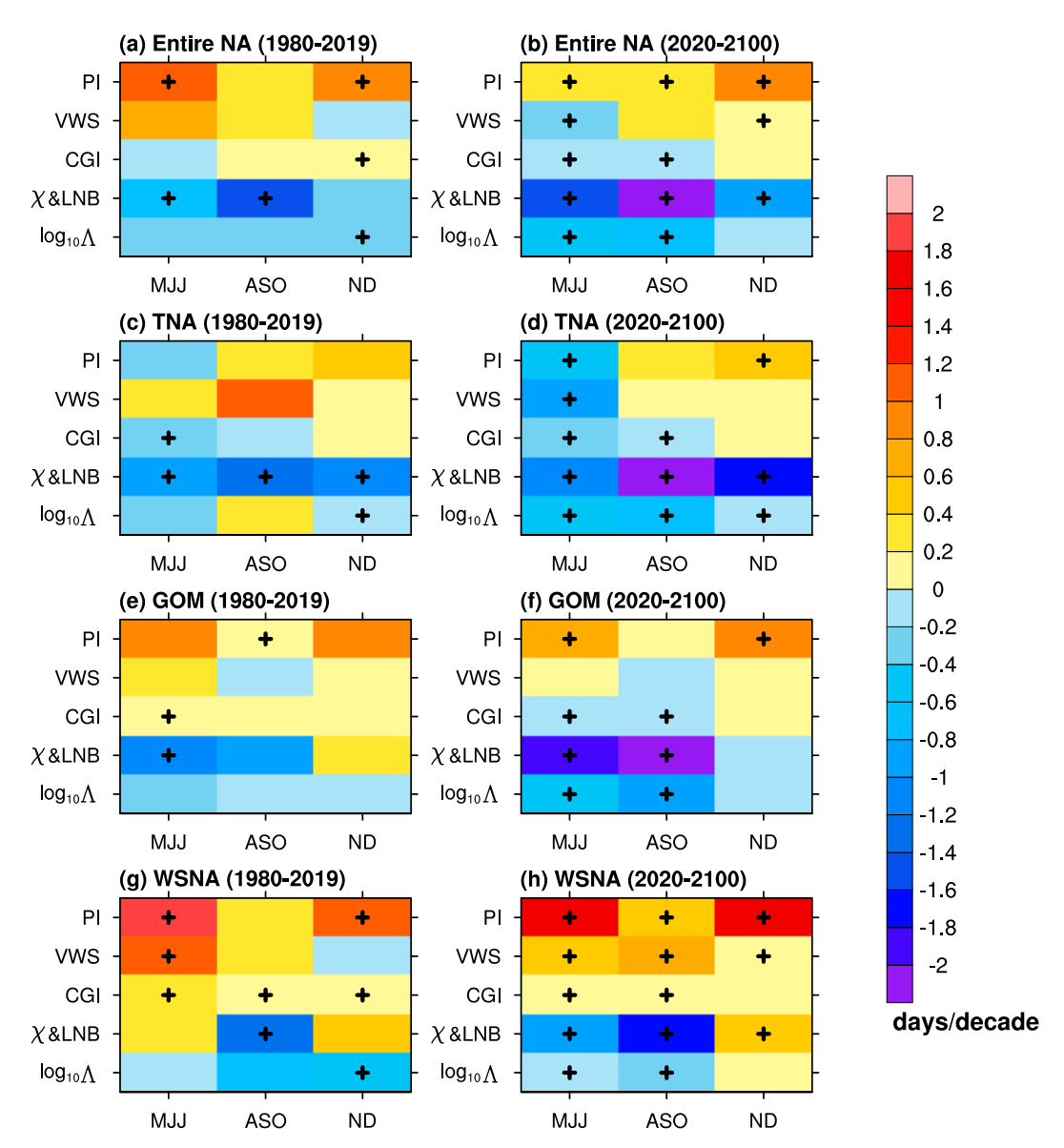


FIG. 11. As in Fig. 9, but for two periods of the coupled high-resolution simulation with CESM. (left) The trend in the number of days with favorable conditions during the period 1980–2019 (forced here with a mixture of observed and projected emissions; see text for details). (right) The trend from 2020 to 2100, continuing under the RCP8.5 projection. The crosses represent trends that are statistically significant (p < 0.10) during the period.

first-century simulation, with large increases in the central and midlatitude Atlantic. The length of the season that features high PI values becomes longer through the subtropics and middle latitudes of the NA across the simulation of the remainder of this century.

As the climate warms, a potential barrier to tropical cyclone formation rises: the strength of the thermodynamic disequilibrium at the surface usually grows with warming, but not as rapidly as the exponentially increasing saturation deficit (if relative humidity remains the same) in the midtroposphere (e.g., Emanuel et al. 2010; Korty et al. 2017). The ratio of midtropospheric entropy deficits to surface disequilibrium,

as measured by χ , increases with warming, which is deleterious to tropical cyclone formation and intensification. Time series of χ show that it rises in all months of the season in the high-resolution simulation through 2100 (graphs not shown).

Figure 11 shows trends in the number of days with favorable values of each environmental parameter across the entire basin (top row) and in subregions of the basin; trends that are statistically significant (p < 0.10) are marked with a cross. In the portion of this simulation overlapping with the period examined in the reanalyses (left column; 1980–2019), there are statistically significant increases in the number of days featuring high values of PI in the early and late months of the season when integrated

over the entire NA and when integrated over the WSNA; there is also a statistically significant increase in the GOM during ASO. Trends in PI are generally upward in the other subregions and in other months, although not significantly. Given that the period 1980-2019 was forced with a mixture of observed emissions and projections, direct comparisons with the behavior in Fig. 9 should be treated with caution. Yet there are strong similarities in the increase of PI across the full basin and in the subregions examined: the sign of the increase in each part of the season (early, middle, and late) and in each subregion of the basin matches the sign of trends in ERA5 (higher in all cases, except for MJJ in the TNA). The trends are statistically significant in both ERA5 and in CESM during ND in the full basin, in ASO in the GOM, and in MJJ and in ND in the WSNA. Further trends toward high PI are projected to continue through 2100 (right columns) in the basin as a whole and in most months in the three subregions.

There is less coherence between the sign of VWS changes in this simulation and what was found with the reanalyses, but most of the trends both in CESM and in the reanalyses are insignificant for the period of 1980–2019. As noted above, there is a consistent decrease in days with favorable χ in the CESM simulation, which and continues under the projections to 2100. In the reanalyses, most trends in χ were insignificant between 1980 and 2019 and the sign was in several instances inconsistent between ERA5 and MERRA-2. Because there are fewer days with low χ in warmer climates, measures like the ventilation index, which incorporate χ , are most often driven toward fewer days with favorable values in most months and subregions. The common thread observed in this simulation and in the reanalyses is an expansion in coverage of high PI especially in subtropical latitudes in all months of the season. This is consistent with results reported by Dwyer et al. (2015) and in several model analyses (e.g., Ting et al. 2015, 2019).

5. Conclusions

We analyzed two high-resolution reanalysis products and found several changes in large-scale environmental factors consistent with the lengthening of the North Atlantic TC season reported between 1980 and 2019. Days with high PI become more frequent in subtropical and midlatitude parts of the basin, and there are statistically significant increases in the WSNA in the early, middle, and late months of the season in both ERA5 and MERRA-2 datasets (see Figs. 9g,h). There is also a statistically significant increase in the number of days with high PI in the GOM during the early and middle months of the season in both datasets. There are increases in the TNA later in the storm season (ASO in both ERA5 and MERRA-2; ND also in MERRA-2), and across the entire basin there are statistically significant increases in the number of days with high PI. Projections from a high-resolution simulation for the remainder of the twenty-first century showed the number of days with high PI is likely to continue increasing in the GOM and WSNA, which leads to a trend of a longer season of favorable PI in subtropical latitudes.

The thermodynamic parameter χ is a strong function of temperature, and we found that its calculation is sensitive to both the choices of what pressure levels are used in calculating

boundary layer entropy as well as to subtle differences in boundary layer temperature and humidity values between ERA5 and MERRA-2. This sensitivity can lead to divergent results in some regions and months in metrics like the ventilation index and underscores a need for more careful consideration of this parameter. Indeed, Lee et al. (2020) have shown that a statistical downscaling method that draws on genesis indices can yield wildly divergent results in TC activity arise if relative humidity is used in the index in place of χ . Emanuel et al. (2010) introduced χ into an updated genesis index, arguing that it might explain the decreases in TC counts modeled in CMIP3 and CMIP5 simulations. Yet in the years since, it has become clear that downscaling methods that draw on environmental conditions produce more storms in hotter climates forced by higher carbon dioxide levels (Emanuel 2013; Korty et al. 2017; Emanuel 2021). Thus, we feel more attention to the role this parameter plays in setting the climatology of TCs is warranted. More broadly, how important changes in humidity are to the count and intensity of TCs, and how best to represent this dependency in environmental indices, are questions worthy of more careful examination.

Acknowledgments. We thank the China Scholarship Council (CSC) and the International Laboratory for High-Resolution Earth System Prediction for support of this study. We thank three anonymous reviewers for their constructive comments, which greatly improved the original draft of this paper.

Data availability statement. The best track data are from www.nhc.noaa.gov/data/hurdat/hurdat2-1851-2019-052520.txt. The 6-hourly ERA5 data used in this study are downloaded from https://cds.climate.copernicus.eu/cdsapp#!/dataset/10.24381/cds.bd0915c6?tab=form and the MERRA-2 data from https://doi.org/10.5067/A7S6XP56VZWS.

REFERENCES

Bister, M., and K. A. Emanuel, 1998: Dissipative heating and hurricane intensity. *Meteor. Atmos. Phys.*, 65, 233–240, https://doi.org/10.1007/BF01030791.

—, and —, 2002: Low frequency variability of tropical cyclone potential intensity 1. Interannual to interdecadal variability. *J. Geophys. Res.*, **107**, 4801, https://doi.org/10.1029/2001JD000776.

Bruyère, C. L., G. J. Holland, and E. Towler, 2012: Investigating the use of a genesis potential index for tropical cyclones in the North Atlantic basin. *J. Climate*, **25**, 8611–8626, https://doi.org/10.1175/JCLI-D-11-00619.1.

Camargo, S. J., M. K. Tippett, A. H. Sobel, G. A. Vecchi, and M. Zhao, 2014: Testing the performance of tropical cyclone genesis indices in future climates using the HiRAM model. *J. Climate*, 27, 9171–9196, https://doi.org/10.1175/JCLI-D-13-00505.1.

—, and Coauthors, 2020: Characteristics of model tropical cyclone climatology and the large-scale environment. *J. Climate*, 33, 4463–4487, https://doi.org/10.1175/JCLI-D-19-0500.1.

Dwyer, J. G., M. Biasutti, and A. H. Sobel, 2012: Projected changes in the seasonal cycle of surface temperature. *J. Climate*, 25, 6359–6374, https://doi.org/10.1175/JCLI-D-11-00741.1.

- —, and —, 2014: The effect of greenhouse gas–induced changes in SST on the annual cycle of zonal mean tropical precipitation. *J. Climate*, **27**, 4544–4565, https://doi.org/10.1175/JCLI-D-13-00216.1.
- —, S. J. Camargo, A. H. Sobel, M. Biasutti, K. A. Emanuel, G. A. Vecchi, M. Zhao, and M. K. Tippett, 2015: Projected twenty-first-century changes in the length of the tropical cyclone season. J. Climate, 28, 6181–6192, https://doi.org/10.1175/ JCLI-D-14-00686.1.
- Emanuel, K. A., 1986: An air–sea interaction theory for tropical cyclones. Part I: Steady-state maintenance. *J. Atmos. Sci.*, **43**, 585–605, https://doi.org/10.1175/1520-0469(1986)043<0585: AASITF>2.0.CO;2.
- ——, 1987: The dependence of hurricane intensity on climate. Nature, 326, 483–485, https://doi.org/10.1038/326483a0.
- —, 1989: The finite-amplitude nature of tropical cyclogenesis. *J. Atmos. Sci.*, **46**, 3431–3456, https://doi.org/10.1175/1520-0469(1989) 046<3431:TFANOT>2.0.CO;2.
- —, 1995: The behavior of a simple hurricane model using a convective scheme based on subcloud-layer entropy equilibrium.
 J. Atmos. Sci., 52, 3960–3968, https://doi.org/10.1175/1520-0469(1995)052<3960:TBOASH>2.0.CO;2.
- —, 2010: Tropical cyclone activity downscaled from NOAA-CIRES reanalysis, 1908–1958. *J. Adv. Model. Earth Syst.*, **2** (1), https://doi.org/10.3894/JAMES.2010.2.1.
- —, 2013: Downscaling CMIP5 climate models shows increased tropical cyclone activity over the 21st century. *Proc. Natl. Acad. Sci. USA*, **110**, 12219–12224, https://doi.org/10.1073/pnas.1301293110.
- ——, 2021: Response of global tropical cyclone activity to increasing CO₂: Results from downscaling CMIP6 models. *J. Climate*, 34, 57–70, https://doi.org/10.1175/JCLI-D-20-0367.1.
- —, and D. S. Nolan, 2004: Tropical cyclone activity and global climate. 26th Conf. on Hurricanes and Tropical Meteorology, Miami, FL, Amer. Meteor. Soc., 240–241.
- —, and A. Sobel, 2013: Response of tropical sea surface temperature, precipitation, and tropical cyclone–related variables to changes in global and local forcing. *J. Adv. Model. Earth Syst.*, 5, 447–458, https://doi.org/10.1002/jame.20032.
- —, R. Sundararajan, and J. Williams, 2008: Hurricanes and global warming: Results from downscaling IPCC AR4 simulations. *Bull. Amer. Meteor. Soc.*, 89, 347–368, https://doi.org/10.1175/ BAMS-89-3-347.
- —, K. Oouchi, M. Satoh, H. Tomita, and Y. Yamada, 2010: Comparison of explicitly simulated and downscaled tropical cyclone activity in a high-resolution global climate model. J. Adv. Model. Earth Syst., 2(4), https://doi.org/10.3894/ JAMES.2010.2.9.
- Eyring, V., S. Bony, G. A. Meehl, C. A. Senior, B. Stevens, R. J. Stouffer, and K. E. Taylor, 2016: Overview of the Coupled Model Intercomparison Project Phase 6 (CMIP6) experimental design and organization. *Geosci. Model Dev.*, 9, 1937–1958, https://doi.org/10.5194/gmd-9-1937-2016.
- Gelaro, R., and Coauthors, 2017: The Modern-Era Retrospective Analysis for Research and Applications, version 2 (MERRA-2). *J. Climate*, **30**, 5419–5454, https://doi.org/10.1175/JCLI-D-16-0758.1.
- Gray, W. M., 1968: Global view of the origin of tropical disturbances and storms. *Mon. Wea. Rev.*, **96**, 669–700, https://doi.org/10.1175/1520-0493(1968)096<0669:GVOTOO>2.0.CO;2.
- —, 1975: Tropical cyclone genesis. Dept. of Atmospheric Science Paper 234, Colorado State University, 121 pp.

- —, 1979: Hurricanes: Their formation, structure and likely role in the tropical circulation. *Meteorology over the Tropical Oceans*, Royal Meteorological Society, 155–218.
- Gualdi, S., E. Scoccimarro, and A. Navarra, 2008: Changes in tropical cyclone activity due to global warming: Results from a high-resolution coupled general circulation model. *J. Climate*, 21, 5204–5228, https://doi.org/10.1175/2008JCLJ1921.1.
- Guan, B., D. E. Waliser, and F. M. Ralph, 2018: An intercomparison between reanalysis and dropsonde observations of the total water vapor transport in individual atmospheric rivers. J. Hydrometeor., 19, 321–337, https://doi.org/10.1175/JHM-D-17-0114.1.
- Haarsma, R. J., and Coauthors, 2016: High Resolution Model Intercomparison Project (HighResMIP). Geosci. Model Dev., 9, 4185–4208, https://doi.org/10.5194/gmd-9-4185-2016
- Karloski, J. M., and C. Evans, 2016: Seasonal influences upon and long-term trends in the length of the Atlantic hurricane season. J. Climate, 29, 273–292, https://doi.org/10.1175/JCLI-D-15-0324.1.
- Kim, H. M., P. J. Webster, and J. A. Curry, 2009: Impact of shifting patterns of Pacific Ocean warming on North Atlantic tropical cyclones. *Science*, 325, 77–80, https://doi.org/10.1126/ science.1174062.
- Knutson, T. R., and Coauthors, 2010: Tropical cyclones and climate change. *Nat. Geosci.*, 3, 157–163, https://doi.org/ 10.1038/ngeo779.
- Korty, R. L., S. J. Camargo, and J. Galewsky, 2012a: Tropical cyclone genesis factors in simulations of the Last Glacial Maximum. J. Climate, 25, 4348–4365, https://doi.org/10. 1175/JCLI-D-11-00517.1.
- —, —, and —, 2012b: Variations in tropical cyclone genesis factors in simulations of the Holocene epoch. *J. Climate*, **25**, 8196–8211, https://doi.org/10.1175/JCLI-D-12-00033.1.
- —, K. A. Emanuel, M. Huber, and R. A. Zamora, 2017: Tropical cyclones downscaled from simulations with very high carbon dioxide levels. *J. Climate*, 30, 649–667, https://doi.org/10.1175/JCLI-D-16-0256.1.
- Kossin, J. P., 2008: Is the North Atlantic hurricane season getting longer? *Geophys. Res. Lett.*, 35, L23705, https://doi.org/10. 1029/2008GL036012.
- —, T. L. Olander, and K. R. Knapp, 2013: Trend analysis with a new global record of tropical cyclone intensity. *J. Climate*, **26**, 9960–9976, https://doi.org/10.1175/JCLI-D-13-00262.1.
- —, K. A. Emanuel, and G. A. Vecchi, 2014: The poleward migration of the location of tropical cyclone maximum intensity. Nature, 509, 349–352, https://doi.org/10.1038/nature13278.
- Landsea, C. W., B. A. Harper, K. Hoarau, and J. A. Knaff, 2006: Can we detect trends in extreme tropical cyclones? *Science*, 313, 452–454, https://doi.org/10.1126/science.1128448.
- Lawton, Q. A., R. L. Korty, and R. A. Zamora, 2021: Tropical cyclones downscaled from simulations of the Last Glacial Maximum. J. Climate, 34, 659–674, https://doi.org/10.1175/ JCLI-D-20-0409.1.
- Lee, C.-Y., S. J. Camargo, A. H. Sobel, and M. K. Tippett, 2020: Statistical-dynamical downscaling projections of tropical cyclone activity in a warming climate: Two diverging genesis scenarios. *J. Climate*, 33, 4815–4834, https://doi. org/10.1175/JCLI-D-19-0452.1.
- Li, M., and Coauthors, 2020: An examination of the predictability of tropical cyclone genesis in high-resolution coupled models with dynamically downscaled coupled data assimilation

- initialization. Adv. Atmos. Sci., **37**, 939–950, https://doi.org/10. 1007/s00376-020-9220-9.
- Luo, B., P. J. Minnett, M. Szczodrak, N. R. Nalli, and V. R. Morris, 2020: Accuracy assessment of MERRA-2 and ERA-Interim sea surface temperature, air temperature, and humidity profiles over the Atlantic Ocean using AEROSE measurements. *J. Climate*, 33, 6889–6909, https://doi.org/10.1175/JCLI-D-19-0955.1.
- McGauley, M. G., and D. S. Nolan, 2011: Measuring environmental favorability for tropical cyclogenesis by statistical analysis of threshold parameters. *J. Climate*, 24, 5968–5997, https://doi.org/10.1175/2011JCLI4176.1.
- Menkes, C. E., M. Lengaigne, P. Marchesiello, N. C. Jourdain, E. M. Vincent, J. Lefèvre, F. Chauvin, and J.-F. Royer, 2012: Comparison of tropical cyclogenesis indices on seasonal to interannual timescales. *Climate Dyn.*, 38, 301–321, https://doi. org/10.1007/s00382-011-1126-x.
- Morris, V., and Coauthors, 2006: Measuring trans-Atlantic aerosol transport from Africa. *Eos, Trans. Amer. Geophys. Union*, **87**, 565–571, https://doi.org/10.1029/2006EO500001.
- Nalli, N. R., and Coauthors, 2011: Multiyear observations of the tropical Atlantic atmosphere: Multidisciplinary applications of the NOAA aerosols and ocean science expeditions. *Bull. Amer. Meteor. Soc.*, 92, 765–789, https://doi. org/10.1175/2011BAMS2997.1.
- Nolan, D. S., 2011: Evaluating environmental favorableness for tropical cyclone development with the method of pointdownscaling. J. Adv. Model. Earth Syst., 3, M08001, https:// doi.org/10.1029/2011MS000063.
- Palmén, E., 1948: On the formation and structure of tropical cyclones. *Geophysica*, **3**, 26–38.
- Rios-Berrios, R., and R. D. Torn, 2017: Climatological analysis of tropical cyclone intensity changes under moderate vertical wind shear. *Mon. Wea. Rev.*, 145, 1717–1738, https://doi.org/ 10.1175/MWR-D-16-0350.1.
- Robertson, F. R., M. G. Bosilovich, and J. B. Roberts, 2016: Reconciling land–ocean moisture transport variability in reanalyses with *P* ET in observationally driven land surface models. *J. Climate*, **29**, 8625–8646, https://doi.org/10.1175/JCLI-D-16-0379.1.
- Royer, J. F., F. Chauvin, and B. Timbal, 1998: A GCM study of the impact of greenhouse gas increase on the frequency of occurrence of tropical cyclones. *Climatic Change*, 38, 307–343, https:// doi.org/10.1023/A:1005386312622.

- Sobel, A. H., S. J. Camargo, T. M. Hall, C.-Y. Lee, M. K. Tippett, and A. A. Wing, 2016: Human influence on tropical cyclone intensity. *Science*, 353, 242–246, https://doi.org/10.1126/science. aut6574
- Tang, B., and K. Emanuel, 2012: A ventilation index for tropical cyclones. *Bull. Amer. Meteor. Soc.*, 93, 1901–1912, https://doi. org/10.1175/BAMS-D-11-00165.1.
- —, and S. J. Camargo, 2014: Environmental control of tropical cyclones in CMIP5: A ventilation perspective. *J. Adv. Model. Earth Syst.*, 6, 115–128, https://doi.org/10.1002/2013MS000294.
- Tang, B. H., and J. D. Neelin, 2004: ENSO influence on Atlantic hurricanes via tropospheric warming. *Geophys. Res. Lett.*, 31, L24204, https://doi.org/10.1029/2004GL021072.
- Ting, M., S. J. Camargo, C. Li, and Y. Kushnir, 2015: Natural and forced North Atlantic hurricane potential intensity changes in CMIP5 models. J. Climate, 28, 3926–3942, https://doi.org/10. 1175/JCLI-D-14-00520.1.
- —, J. P. Kossin, S. J. Camargo, and L. Cuihua, 2019: Past and future hurricane intensity change along the U.S. East Coast. Sci. Rep., 9, 7795, https://doi.org/10.1038/s41598-019-44252-w.
- Tippett, M. K., S. J. Camargo, and A. H. Sobel, 2011: A Poisson regression index for tropical cyclone genesis and the role of large-scale vorticity in genesis. *J. Climate*, 24, 2335–2357, https://doi.org/10.1175/2010JCLI3811.1.
- Vecchi, G., C. Landsea, W. Zhang, G. Villarini, and T. Knutson, 2021: Changes in Atlantic major hurricane frequency since the late-19th century. *Nat. Commun.*, 12, 4054, https://doi.org/ 10.1038/s41467-021-24268-5.
- Vergados, P., A. J. Mannucci, and C. O. Ao, 2014: Assessing the performance of GPS radio occultation measurements in retrieving tropospheric humidity in cloudiness: A comparison study with radiosondes, ERA-Interim, and AIRS data sets. *J. Geophys. Res. Atmos.*, 119, 7718–7731, https://doi.org/10. 1002/2013JD021398.
- Wong, M. L. M., and J. C. L. Chan, 2004: Tropical cyclone intensity in vertical wind shear. J. Atmos. Sci., 61, 1859–1876, https://doi.org/10.1175/1520-0469(2004)061<1859:TCIIVW>2. 0.CO:2.
- Zheng, Y., L. Wu, H. Zhao, X. Zhou, and Q. Liu, 2020: Simulation of extreme updrafts in the tropical cyclone eyewall. *Adv. Atmos. Sci.*, **37**, 781–792, https://doi.org/10.1007/s00376-020-9197-4.